

ABSTRACT

Title of Document: VARIABLE FENESTRATION OF A
3D NANOPRINTED LIVER SINUSOID ON A CHIP

Cara Brainerd, Viswanath Gorti, Morgan Janes
Katherine Jones, Shireen Khayat, Andrew Liu
Madeleine Noonan-Shueh, Sahana Rao

Directed by: Dr. Ryan D. Sochol
Department of Mechanical Engineering

Here we report a novel strategy for engineering liver sinusoids with designed fenestrae that yield near uniform microfluidic flow conditions along the length of the microstructure – capabilities enabled by the use two-photon direct laser writing (DLW). To better model organ systems, researchers have increasingly investigated the use of DLW as a promising means for mimicking both architectures and length scales of physiological components. DLW-based approaches could enable liver sinusoids to be recreated *in vitro*; however, recent efforts to construct permeated tubules exhibit dramatic decreases in fluid flow through the pores downstream. To overcome such issues, here we applied microfluidic circuit theory and in-situ DLW (isDLW) to manufacture liver sinusoids that included fenestrae with distinct sizes to better maintain a consistent fenestra-specific flow profile. Specifically, fenestrae radii were increased from $0.75\ \mu\text{m}$ to $2.01\ \mu\text{m}$ over the length of a $510\text{-}\mu\text{m}$ sinusoid. Theoretical results revealed that the flow rate through the fenestrae could be more maintained along the length of the optimized sinusoid versus the unoptimized sinusoid with uniform fenestrae

which results in inconsistent fluid flow. Preliminary results revealed successful isDLW fabrication of the optimized sinusoid, with proof-of-concept microfluidic flow demonstrations that suggest that the presented strategy could benefit numerous biomedical applications. These results suggest the potential of this design strategy for liver on-a-chip modeling, and given the numerous anatomical structures similar to the presented fenestrated sinusoid, this approach could be extended to model additional organ systems of the body for disease modeling and drug screening.

**VARIABLE FENESTRATION OF A 3D NANOPRINTED
LIVER SINUSOID ON A CHIP**

By

Team MICRO

Cara Brainerd

Viswanath Gorti

Morgan Janes

Katherine Jones

Shireen Khayat

Andrew Liu

Madeleine Noonan-Shueh

Sahana Rao

Thesis submitted in partial fulfillment of the requirements of the
Gemstone Program

University of Maryland, College Park

2019

Advisory Board:

Dr. Ryan D. Sochol, Mentor

Dr. Abhay Andar

Dr. Eric Hoppmann

Dr. Bhushan Mahadik

Dr. Margaret Scull

© Copyright by
Team Micro
2019

Acknowledgements

We would like to express our appreciation to the following individuals who helped us over the course of our research. Thank you to Dr. Ryan Sochol, our Gemstone mentor, for his guidance over the past four years. Thank you to Dr. Margaret Scull, who advised us immensely on the biological applications and details of our research. Thank you to Andrew Lamont, Abdullah Alsarhan, Michael Restaino, and the Bioinspired Advanced Manufacturing Lab for their guidance on our work. Thank you to Caroline McCue and the Terrapin Works Research Prototyping Laboratory. Thank you to John Abrahams, Mark Lecates, and the Micro and Nano Fabrication Laboratory for providing training on equipment needed for our research. Thank you to Jiancun Rao at the Advanced Imaging and Microscopy Laboratory for providing assistance with the scanning electron microscope. Thank you to Nedelina Tchangalova and the University of Maryland Libraries for advising the writing of our proposal and thesis. Thank you to the Gemstone Program staff for their assistance in providing us an opportunity to conduct this research, including Dr. Frank Coale, Dr. Kristan Skendall, Vickie Hill, Leah Tobin, and Jessica Lee.

Table of Contents

1	Introduction	1
2	Literature Review	4
2.1	Drug Development	4
2.1.1	Current Problems in Drug Development	4
2.1.2	Importance of Liver in Drug Development	5
2.1.3	Liver Bioarchitecture	6
2.2	Microfluidic Models	7
2.2.1	Liver on a Chip	9
2.2.2	Previous Experimental Applications of Liver-on-a-Chip Technology	12
2.3	Additive Manufacturing	15
2.3.1	Additive Manufacturing Methods	16
2.3.2	Nanoscribe	18
3	Methodology	21
3.1	Proposed Model	21
3.2	Theoretical Methodology	23
3.3	Fabrication Methodology	30
3.4	Microfluidic Device Manufacturing	31
3.4.1	Negative Mold Manufacturing	31
3.4.2	Micromolding	32
3.4.3	Glass Bonding	33
3.4.4	Sol-Gel Coating	33
3.4.5	Vacuum Loading of Photoresist	34
3.4.6	Microarchitecture Fabrication	34
3.4.7	Scanning Electron Microscopy	36
3.5	Fluid Flow Testing	36
3.5.1	Flow Visualization in 3D Printed Tubules	36
3.5.2	Leakage Test	38

4	Results	39
4.1	Theoretical Results	39
4.2	Device Fabrication	43
4.3	Proof of Concept Studies	45
4.4	Barrier Tests	47
4.5	Solid Tubules	48
4.6	Unoptimized and Optimized Tubules	50
4.7	Fluid Flow Testing	54
5	Discussion	56
5.1	Theoretical Results	56
5.2	Fabrication Results	58
5.3	Printing Results	60
5.4	Experimental Verification of Designed Fenestrae	61
5.5	Future Work	62
6	Conclusion	66
7	Appendices	68
A	MATLAB Code	68
8	Glossary	72

List of Tables

1	Custom MATLAB program inputs used for design of an optimized microfluidic tubule.	29
2	Custom MATLAB program outputs used for design of an optimized microfluidic tubule.	29
3	User-specified parameters for design of an optimized microfluidic tubule.	39
4	User-specified values of input parameters related to fluid flow.	42

List of Figures

1	Diagram of liver lobule	6
2	Cell differentiation in 3D cultures	7
3	Lung on a chip microfluidic device	9
4	Liver-on-a-chip model that mimics the hepatic cords of the liver	11
5	Paracrine signaling in the liver	13
6	Methods of 3D printing	16
7	Printing resolutions of the Photonic Professional GT Nano- scribe printer	19
8	CAD renderings of proposed model	22
9	Circuit theory representation of fenestrated tubule	25
10	Circuit theory model of pipe flow through a fenestrated tubule containing three sets of pores.	27
11	Device fabrication process	31
12	Diagram of sol-gel coating	34
13	Fluigent MFCS-EZ system and Maesflo software used for fluid flow testing	37
14	Plot of pore radius as a function of pore row number in the optimized tubule	41
15	CAD renderings of unoptimized and optimized tubules	41
16	Fluid velocity and magnitude plots	42
17	Plot of percent decrease in volumetric output flow rate as a function of pore row number	43
18	Microfluidic device fabrication	44
19	Central chamber of the microfluidic device	45
20	Printing studies with Ormocomp	46
21	Printing studies with IP-L 780	47
22	H-shaped microfluidic device showing sol-gel coating	48
23	Fluid application to parallel channels results	48
24	CAD rendering of solid tubule and tubule with block ends	49

25	Cross-shaped microfluidic device showing sol-gel coating . . .	50
26	CAD rendering of unoptimized tubule	51
27	Unoptimized tubule inside a microfluidic device	52
28	CAD rendering of the optimized tubule	53
29	Optimized tubule inside a microfluidic device	53
30	View of pores in the optimized microchannel	54
31	Fluid testing results	54
32	CAD rendering of triangular channel mold	59
33	3D printed mold with triangular channels	59
34	CAD representation of future model	62

1 Introduction

The Food and Drug Administration requires that candidate medications meet several requirements before approval and dissemination to the market. These candidate medications must prove to be both efficacious and nontoxic at each of the main phases in the drug development process: *in-vitro* or cell-based tests, *in-vivo* or animal models, and then finally multiple clinical trials. On average it takes over two billion dollars and over a decade for one drug to come out of this system [1]. This high cost is associated with significant failure rates, many of which are due to problems with liver toxicity [2].

The liver is primarily responsible for metabolism and filtration of the bloodstream [3]. The metabolism of drugs in the body is done by the liver, which is essential to consider in clinical drug testing. Novel drugs cannot be approved if the drug and its metabolites are too toxic to liver cells [2]. Therefore, we aim to develop an organ-on-a-chip liver sinusoid model that can mimic microarchitectures in the liver and expedite this screening process.

The model will be structured similarly to the liver sinusoid, which was selected due to its role as the center of drug processing in the liver [4]. The liver is made up of functional liver lobule subunits. Each lobule contains sinusoids which are fenestrated microchannels that transport nutrient-rich blood to the surrounding hepatocytes, the primary cells of the liver [5]. This arrangement allows hepatocytes to effectively metabolize drugs and

nutrients in the bloodstream [5].

Traditional *in-vitro* models used in preliminary drug testing include Petri dishes and multiwell plates. These conventional models lack certain characteristics of physiological microenvironments [6]. These include static fluidic conditions, inaccurate length scales, limitation to culturing a single type of cell line, lack of mechanical stimuli, and flat “two-dimensional” architecture [6]. The organ-on-a-chip field aims to address these issues. While state-of-the-art models have addressed fluidic flow, more accurate length scales, allowance for up to two cell type monolayers, mechanical stimuli, these still have flat “two-dimensional” architecture [6]. Recent additive manufacturing advancements that allow for the fabrication of structures on the order of nanometers have the potential to advance the field through the production of nanoscale models that capture even the smallest features of organ physiology [7]. The goal of this project is to use microfluidics and state of the art laser lithography technology to produce an organ-on-a-chip model of the liver that will result in cellular behavior comparable to that of a human liver.

The two central questions that motivate this research are:

- 1. Can an engineered microtubule with designed fenestrae yield near-uniform microfluidic flow conditions along the length of the microstructure?*
- 2. How does the integration of this engineered microtubule influence liver cell function?*

We hypothesize that by using fluid modeling and direct laser writing

(DLW) nano3D printing techniques, we can determine fenestrae of varied sizes at specific points along the microstructure that optimize uniform fluid flow through the tubules and fenestrae. Additionally, we hypothesize that by mimicking the microarchitecture of a liver sinusoid and therefore mimicking the specific microenvironment of the liver sinusoid, liver cell function will be more comparable to physiological conditions as opposed to traditional *in-vitro* models.

2 Literature Review

2.1 Drug Development

2.1.1 Current Problems in Drug Development

As researchers synthesize potential drugs to improve the current methods of treatments for various diseases, the FDA must determine the degree of human toxicity before the drug is released on the market. *In-vitro* toxicity testing is the scientific analysis of toxic substances on mammalian cell lines. This preliminary testing is primarily used to identify hazardous properties of potentially useful new pharmaceuticals [8]. The main goal of *in-vitro* drug toxicity testing is to model the complex sequence of physiological events in which interactions between cells and drugs, drug metabolites, and drug protein conjugates may potentially lead to tissue damage. However, the level of molecular detail in metabolic processing is rarely captured in current *in-vitro* cell culture models: new chemical compounds often fail during late-stage human drug testing and can receive “black box” warnings, which indicate that there are life threatening risks associated with the medication and it is therefore not U.S. FDA approved [9]. One example of these warnings is drug induced liver injury (DILI), which is a major reason for drug failures in the drug development process [10]. DILI remains the most common cause of acute liver failure in the U.S., accounting for 13% of all acute liver failure cases in 2005 [11]. *In-vitro* cell-based assays and preclinical *in-vivo* studies in animal models are often not adequately able

to forecast potential issues like DILI, which has contributed to the costly and inefficient drug development process.

2.1.2 Importance of Liver in Drug Development

The liver, depicted in Figure 1, is composed of a variety of structures that work together to filter the blood from the digestive tract before circulating it to the rest of the body. The detoxification of chemicals and the metabolism of drugs are two functions of the liver that are critical in the maintenance of homeostasis in the body [3]. The liver consists of cells called hepatocytes, which house these detoxification and filtration processes [12]. Hepatocytes are often grown in petri dishes to test drug toxicology and measure the effects of other cell toxins. However, this method is not entirely accurate because there are other structures within the liver, including the sinusoids, hepatic artery, and portal vein that interact with hepatocytes to contribute to liver function. The hepatic artery carries oxygen-rich blood to the liver, while the portal vein delivers nutrient-rich blood from the gastrointestinal tract. In order to achieve proper detoxification of chemicals and metabolism of drugs, the hepatocytes in the liver rely on the flow of blood from these major hepatic blood vessels. The vessels carry the chemicals into the liver, where the hepatocytes then release the enzymes necessary for metabolism [5].

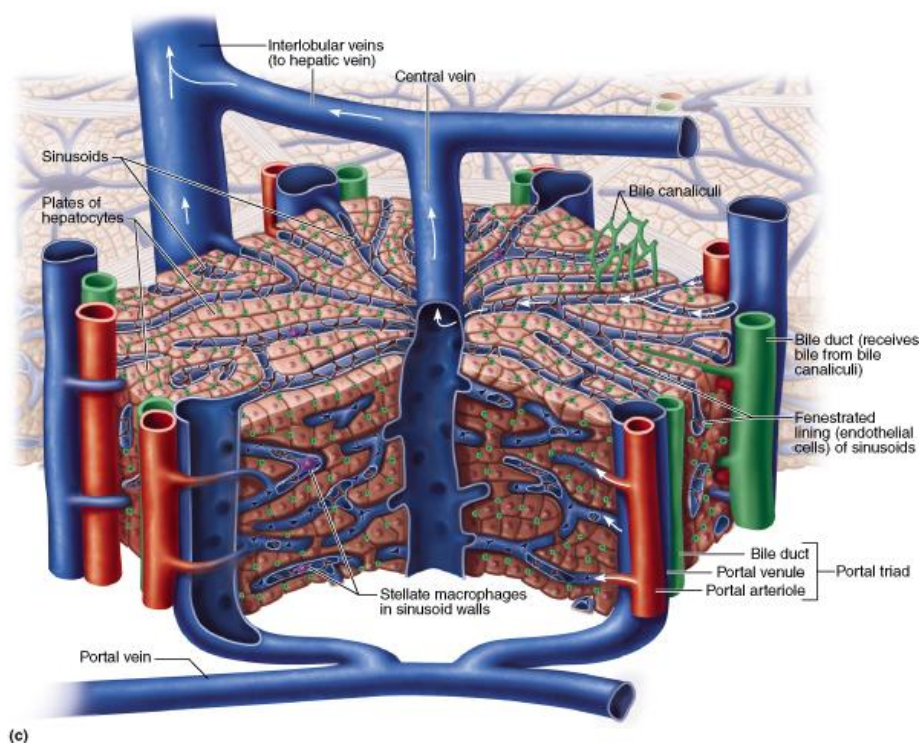


Figure 1: A diagram of a liver lobule highlighting the portal triad and direction of blood flow from the portal vein to the central vein. The sinusoids, represented by thin blue channels, are shown surrounded by hepatocytes organized into plates, or cords [13].

2.1.3 Liver Bioarchitecture

Another important structure is the liver sinusoid. Sinusoids within the liver contain a fenestrated, or porous, internal lining of endothelial cells that allows for the filtering of fluids, particles and solutes between the blood and surrounding hepatocytes. The sinusoids and major vessels of the liver significantly contribute to liver function, which is why such structures have been the main focus of past and current toxicology research efforts for this organ [5]. Current *in-vitro* drug screening methods are unable to accurately predict which compounds are likely to induce drug-related liver injuries due to their inability to promote cellular functions that are critical for drug metabolism [11]. This incongruence can be addressed through the

maintenance of accurate tissue architecture in models for toxicity testing as recapitulating the cellular microenvironment promotes accurate *in-vivo* interactions. Tissue architecture encompasses the interactions of adjacent differentiated cells, extracellular matrix (ECM) components and adhesion molecules, growth factors, Ca^{2+} and ATP concentrations, and local pH [11]. These factors originally determine cell differentiation and enable cell functions such as communication and mobility. Mandin–Darby Canine Kidney (MDCK) cells, thyroid cells, and mammary cells have shown to spontaneously form cysts and tubules in 3D cultures, a physiologically normal response, but are not formed in 2D cultures (Fig. 2) [14]. This demonstrates how the 3D coordination and integration of cellular interactions dictate tissue level functions in terms of assembly and maintenance of homeostasis. Tissue architecture and 3D geometry of the cellular scaffold is necessary for physiologically relevant cellular organization which traditional forms of monocultures lack.

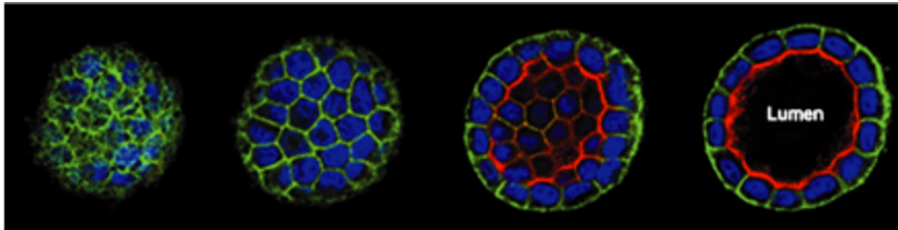


Figure 2: 5 μm sections of spontaneously formed 3D MDCK cultures with a different stain on each biochemical surface [9].

2.2 Microfluidic Models

An organ on a chip is a microfluidic cell culture device that is designed to model the behavior of an organ or organ system. These devices are

typically fabricated using soft lithography or photolithography in a similar way to computer microchips [6]. Traditionally, organ-on-a-chip technology involves culturing cells in hollow microchannels and applying fluid flow to simulate physiological conditions. Researchers may also apply mechanical forces, introduce structural components such as ECM, or include multiple cell lines or tissue interfaces in an organ on a chip to mimic an organ's microenvironment [6]. For example, a lung-on-a-chip device created by researchers at Harvard modeled the alveolar-capillary interface of the lung and included vacuum chambers to simulate the mechanical effects of breathing (Fig. 3). This successful model showed that it was feasible to develop and use organ-on-a-chip systems for *in vitro* study [15]. After the original lung on a chip, various models of other organs were created. One example is the heart on a chip, which was found to better mimic the heart's contractions, yielding advancements in research involving the cardiotoxicity of drugs [16].

Organ-on-a-chip technology is a complementary technology to other 3D cell culture types such as organoids and spheroids that have greatly propelled research in understanding the effects of drugs on certain organs [6]. One important note is that organ-on-a-chip devices do not seek to grow an entire organ, rather, they model the smallest practical unit of an organ to accurately replicate the functions of a system [6]. A developing area of research using organ-on-a-chip technology includes the connection of multiple organ-on-a-chip devices to model organ systems, such as the excretory and renal systems. As this technology advances, researchers hope

to create a human on a chip that incorporates all major organ systems [17, 18]. Organ on a chips have great potential to replicate organ functions of disease. As an example, the lung-on-a-chip device developed was used to investigate pulmonary edema [19]. As time has progressed, organ-on-a-chip devices have only advanced and continue to demonstrate great potential in drug development [19].

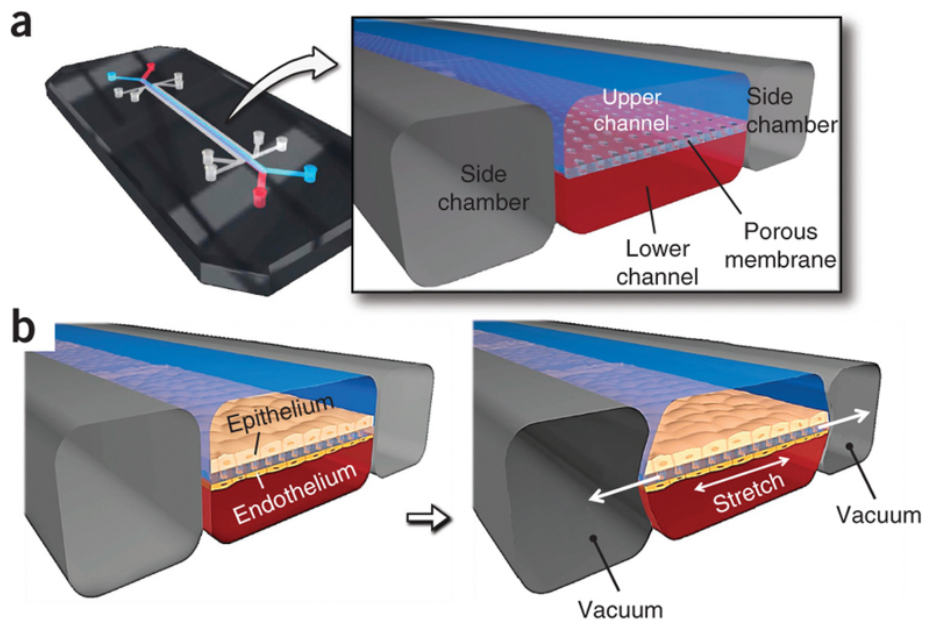


Figure 3: Lung on a chip device with two vacuum chambers on each side. This device recapitulates the alveolar-capillary interface by applying mechanical stresses that mimic the effects of breathing [19].

2.2.1 Liver on a Chip

Compared to traditional 2D models, organ-on-a-chip devices have several important benefits. One advantage is that these devices provide the ability to manipulate the 3D cellular environment [20]. In addition, these devices expose cultured cells to mechanical forces found in the human body, such as fluid flow, tension, and compression, which influence cellular development and interaction [6, 21]. This is in marked contrast to traditional 2D

cultures and even 3D cultures that lack fluid flow [14]. As previously stated, the liver is an important system of interest for organ-on-a-chip modeling due to its role in toxin filtration and drug metabolism [3]. In the past, studies have indicated that liver-on-a-chip devices exhibit greater liver-specific enzymatic activities and responses to chemical stimuli compared to two-dimensional petri dish models [22]. Ultimately, these liver-on-a-chip models share the goal of understanding how liver cells in biologically complex 3D arrangements communicate with one another and with their surroundings, with the ultimate goal of imitating liver function [22]. The use of these structures is an important step in understanding how the human liver responds to drugs and other chemicals, which may lead to the development of an improved *in-vitro* platform for clinical drug testing.

A variety of liver-on-a-chip models have been created using traditional and contemporary 3D fabrication methods. Organ-on-a-chip devices are typically created using soft lithography, enabling complex patterns to be integrated into biologically compatible materials [23]. For example, soft lithography was used to fabricate a device containing a radial pattern of pillar arrays with HepG2 cells in a collagen hydrogel (Fig. 4). This device, which was designed to structurally mimic the hepatic cord-like system of the liver, allowed researchers to quantify metabolic cellular responses to known drug-drug interactions. In addition, it was determined that this model expressed higher levels of enzyme activity than liver cells in 3D culture, indicating that it may be valuable in the clinical drug testing process due to its heightened metabolic activity [22].

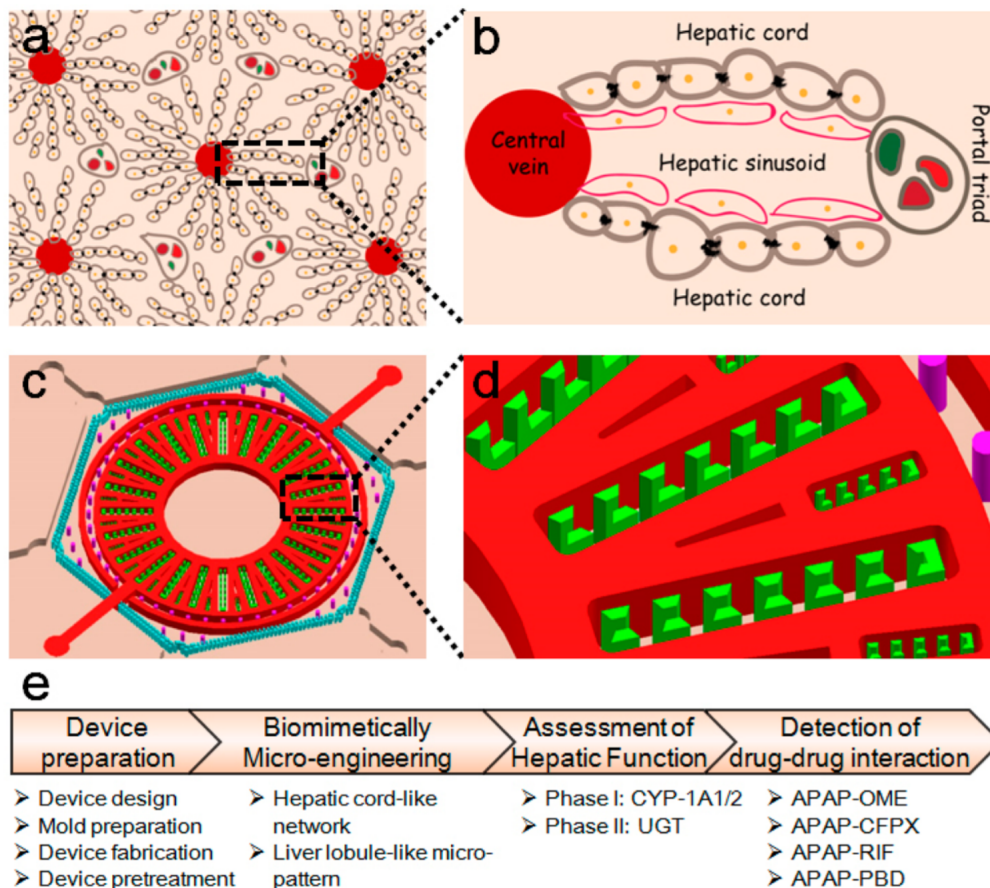


Figure 4: Development of a liver-on-a-chip model that mimics the hepatic cords of the liver. The structure of hepatic cords arranged around the central vein presented in (a) and in more detail in (b) is captured in the microfluidic device in (c). The pillar arrays containing HepG2 cells are displayed in detail in (d) [22].

To accurately replicate the 3D microenvironment of the liver, there are a few basic techniques that most researchers take advantage of in their models. One of the most important is the flow of media, which exposes the cells to shear stresses that are commonly encountered in the body through functions such as breathing and muscle contractions [6]. Most microfluidic devices also use some form of cell patterning, which allows researchers to deposit certain types of cells in specific locations on the device to mimic cellular arrangement in a given organ [6]. This can be achieved through direct cell printing or the incorporation of microchannels, which are also

frequently used to evaluate cell and nutrient transport and facilitate fluid flow. Another important element of the device is the type of cells that are cultured in or on it. One common cell line used to study the liver is a series of biologically immortal Hep G2 cells. Hep G2 cells are also commonly used in studying cytotoxic and genotoxic compounds in the liver and have been studied in liver-on-a-chip devices [22, 24]. Another cell line is the human hepatoma cell line, HepaRG, which retains the expression of many liver-specific functions and enzymes but is still much less expressive than primary hepatocytes, which are the gold standard of *in-vitro* testing [25].

2.2.2 Previous Experimental Applications of Liver-on-a-Chip Technology

Liver-on-a-chip technologies have been used for many applications, such as emulating cell signalling pathways, creating accurate disease models, and containing the spheroids and flow of media (Fig. 5). Metabolic activity and albumin production was discovered to be greater in the co-culture model in comparison to a control that was not exposed to paracrine signaling, signifying that cell-cell interactions may positively affect biological relevance in a liver model [26].

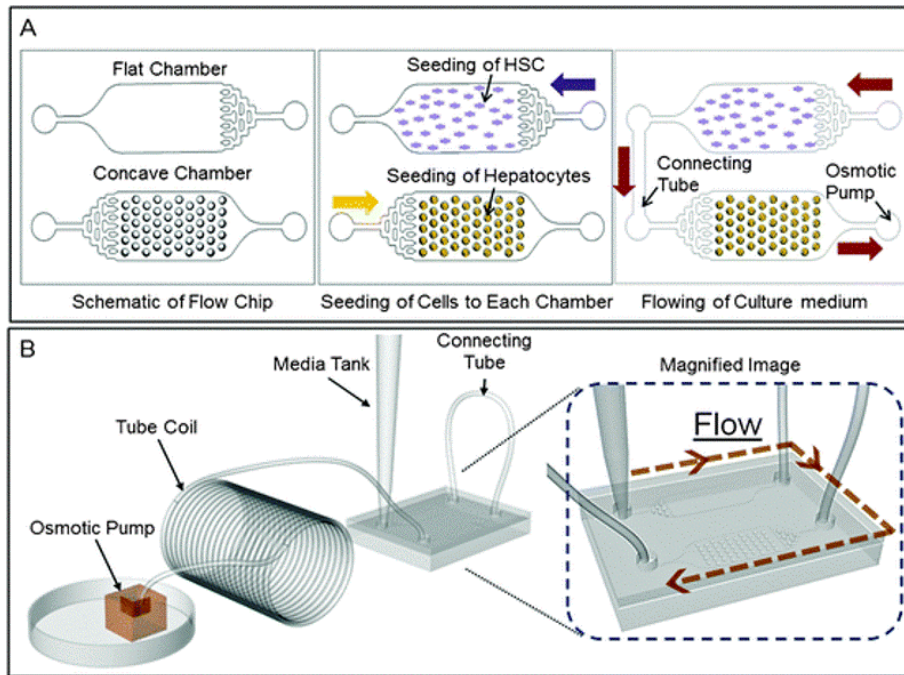


Figure 5: Paracrine signaling in the liver. (a) Design schematic of a concave chamber containing Hep G2 spheroids and a flat chamber containing HSCs. The two chambers were connected to allow media from the HSC chamber to flow to the Hep G2 chamber. (b) Experimental setup containing chambers connected by tubing, a media source, and a connection to an osmotic pump [26].

Liver-on-a-chip devices have also been significant in the research of diseases and syndromes. One implementation of this technology was the creation of an *in vitro* model of an alcohol diseased liver. Liver damage was simulated by exposing spheroids of rat-derived hepatocytes and hepatic stellate cells to differing concentrations of ethanol, then inserting them into the microfluidic device. The chip accurately simulated the diseased liver on the basis of albumin and urea secretion in the models with 60 - 80 μ L exposure to ethanol, and also displayed the onset of fibrosis [27]. This work provides experimental evidence that secretion of albumin and urea may be important indicators of metabolic function in the liver [27]. Liver-on-a-chip models are also being used to research drug interactions inside the body.

One use of liver-on-a-chip technology allowed for drug screening through the analysis of hepatocyte metabolism. A microfluidic device was created to analyze acetaminophen metabolites in relation to hepatic cell cytotoxicity, showing the inverse relationship between acetaminophen concentration and metabolite production [28].

Although some processes mainly require only the function of one organ, other processes do not occur in isolation and thus require the interaction of multiple systems. In one study, nephrotoxic effects of ifosfamide, an anticancer drug, were only observed when a liver-on-a-chip and a kidney-on-a-chip system were connected [29]. Soft lithography was used to create a liver and skin cell co-culture system in a microfluidic organ-on-a-chip device. The co-cultures operated at a steady metabolic rate and the skin cells took up the albumin produced by the hepatocytes [30]. In an extension of this study, intestine, skin, kidney, and liver equivalents were all cultured in a similar microfluidic device. Absorption, distribution, metabolism and excretion profiles were created for the 28 days during which there was homeostasis between the four types of cells, providing data for improved toxicity testing [31].

Yet another microfluidic device was created through soft lithography which compartmentalized four various types of cells: liver, lung, kidney, and adipose cells. The device allowed for fluidic interactions between the cells while limiting crosstalk between the organs, thus allowing supplements like growth factors to only interact with one cell type while not affecting the other cells [32]. This enabled more accurate toxicity modeling of multiple

co-cultures in a microfluidic device, as a single biochemical like TGF- β 1 can be delivered in isolation to enhance the function of a specific cell type like the lung cell line in this example without changing the functions of the other co-cultured cell lines [32]. This illustrates the importance of organ-organ interactions, as the drug was activated in the liver for nephrotoxic effects.

2.3 Additive Manufacturing

In addition to soft lithography, additive manufacturing provides a number of advantages in the development of liver-on-a-chip models. Different types of 3D printers can rapidly fabricate precise structures on the resolution of microns, directly print cells in complex 3D arrangements, and conveniently utilize a variety of materials. By taking advantage of additive manufacturing technology, researchers have been able to emulate the complex microenvironment of human organs with increasing precision. Additive manufacturing (3D printing) produces 3D objects through layering of material aided by a computer program (Fig. 6). This innovative method of printing has been applied to fields such as engineering, manufacturing, art, education, and medicine [33]. Different methods of 3D printing can be utilized depending on desired function and properties of the product.

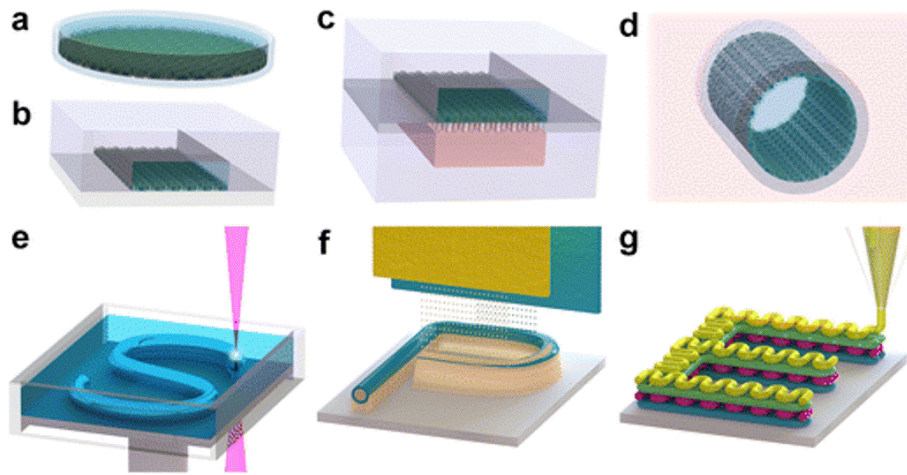


Figure 6: Multiple methods of 3D printing. (a) Traditional petri dish model with a 2D cell monolayer. (b) Single-layer microfluidic system with a 2D cell monolayer and introduction of fluid flow to the model. (c) Multilayer microfluidic system with a 2D cell monolayer on an intervening porous membrane, allowing for more than one cell line to be cultured in one model. (d) Tubular porous membrane with a 3D cell monolayer. (e) Stereolithography (SLA). Focused light induces localized photopolymerization (white) of a photocurable material (blue) to fabricate 3D structures. (f) PolyJet Printing (PJP)/MultiJet Modeling (MJM). Multiple inkjets in parallel deposit microdroplets of photocurable material and sacrificial support material simultaneously to fabricate 3D structures. (g) Extrusion-based printing. Material is extruded through a nozzle and deposited to fabricate 3D structures [34].

2.3.1 Additive Manufacturing Methods

Extrusion-based printing involves the deposition of material in a point-by-point manner through a nozzle [35]. This method has been used to bioprint cell-laden hydrogel 3D structures with built-in microchannels to ultimately produce large-scale organ models [34]. Extrusion-based printing can also involve printing sacrificial material, material that will be removed, or cell compatible material to create 3D microsystems. One basic fabrication procedure for biological constructs involves 3D printing a sacrificial material, applying a liquid cell-compatible material surrounding or inside the sacrificial material, curing the cell-compatible material, and removing

the sacrificial material to leave only the cell-compatible material behind. This type of fabrication is limited in time consumption and geometrical complexity [35, 36]. Polyjet printing dispenses microdroplets of photocurable resins, known as photopolymers, and cures them in thin layers to create a 3D object. This type of printing often requires a sacrificial support material, which can be removed to leave only the photopolymer [35]. A physiologically accurate descending aortic model was created using polyjet printing due to this method's geometrical accuracy, speed, and low cost of production [37]. In a 2016 study, 3D printing techniques were investigated by comparing microfluidic fabrication parameters. Polyjet printing was shown to be superior to other forms of 3D printing based on spatial accuracy, surface roughness measurements, and printing resolutions [27].

Stereolithography is a 3D printing method that incorporates direct laser writing to create microfluidic channels and complex geometric structures [35]. The method involves using focused light to photocure liquid polymers layer by layer, leading to the creation of a 3D structure [38]. This form of 3D printing aided in the study of how 3D microenvironments affect cancer cell growth and movement. Photocurable polyethylene glycol diacrylate was used to create log-pile microarchitectures, allowing for the construction of precise structures through stereolithography. Results showed that both types of cells tested displayed different migration properties in 3D scaffolds compared to 2D scaffolds, demonstrating a difference in physiological accuracy between 3D and 2D models [39].

Laser lithography was used as a stereolithography technique for its abil-

ity to create high resolution structures with dimensions as small as 100 nm through precise photopolymerization by a laser [40]. Because of the precision of laser lithography and the elasticity of the printing material OrmoComp, a biocompatible gel with high chemical and thermal stability, researchers determined forces exerted by primary cardiomyocytes were only observed using complex structures resembling *in vivo* extracellular matrices. However, a limitation of the laser lithography technique is the height constraint of the microscope lenses, which in one study was 80 μm , limiting the size of channels and possibly interfering with physiological length scales [40].

2.3.2 Nanoscribe

The 3D printing machine that will aid in achieving the proposed 3D liver model is the Nanoscribe Photonic Professional GT printer, due to its combination of high resolution (Fig. 7) and the moving beam capabilities of the printer [41]. This machine is optimal for mimicking organ structures because it is able to print in a 200 μm circular area without sacrificing accuracy without the need for a moving base [42]. This capability is derived from the moving beam fixed sample functionality of the printer, allowing structures to be printed on the resolution of micrometers [41]. Because the liver has microarchitectures that directly affect its function, such as its sinusoid channels, the ability for the Nanoscribe to create small biophysical structures makes it an optimal tool for this project [43].

The type of stereolithography the Nanoscribe uses is two photon laser

writing of various UV-curable photoresist materials [41]. Two photon laser writing is caused by ultrashort laser pulses which initiate polymerization of photosensitive material through two photon absorption. After removal of unpolymerized resin, the desired 3D structure remains [44].

There are a variety of biocompatible materials that can be used by the Nanoscribe to print these structures. An alternative to these materials is photopolymerizable biocompatible photoresist that forms a patterned coating on the surface. OrmoComp, a photoresist, was found to support cell growth and rapidly solidify after exposure to 40 minutes of UV radiation [45]. This is a promising biocompatible material with the ability to produce a durable structure, especially for a 3D organ model. Additionally, the machine can also utilize specifically designed negative IP-photoresists that increase the 3D microfabrication capabilities. Negative photoresists keep the areas exposed to the laser while the areas not exposed to the laser can be dissolved. The negative IP-photoresists provided by the Nanoscribe company are able to form 150 nm structures, increase print speed, increase mechanical stability, and decrease mechanical stress during printing [41].

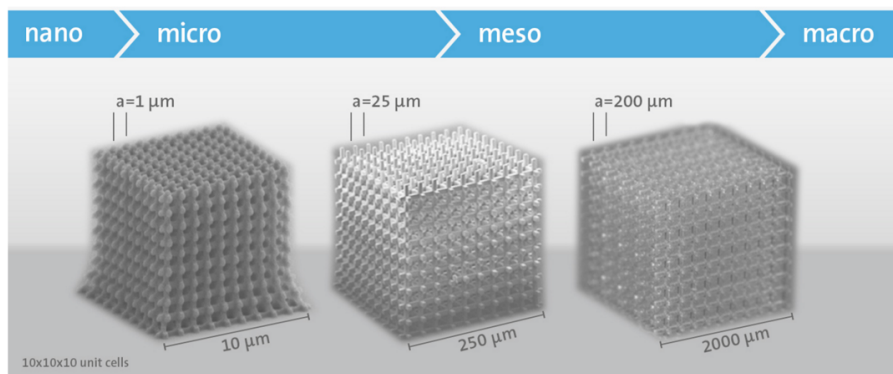


Figure 7: The Photonic Professional GT Nanoscribe printer demonstrates a variety of printing resolutions, varying from the nanoscale ($1 \mu\text{m}$) to the macroscale ($200 \mu\text{m}$) [41].

The Nanoscribe is able to print within the channels of devices made from a variety of materials. One such material, polydimethylsiloxane (PDMS) is a common silicon in soft lithography techniques; however, although it is cost efficient and easily fabricated, its hydrophobicity causes it to be unstable [46]. Another commonly used biomaterial for scaffolding is fibrin hydrogel, prepared from fibrinogen and thrombin. In one study, the hydrogel provided a medium on which cells could adhere and multiply, but it was also found to be too fragile to maintain a 3D structure [47].

3 Methodology

3.1 Proposed Model

This project aimed to fabricate a novel liver-on-a-chip device on a physiologically relevant scale that mimicked *in-vivo* hepatic activity. This device is composed of a cell containment chamber to house cultured hepatocytes, as well as input and output pores for fluid flow (Fig. 8a). In addition, the device included a porous microchannel through the cell chamber representing a liver sinusoid with the ability to diffuse nutrients to surrounding cells (Fig. 8b). This design allows for constant fluid flow throughout the liver model, creating a dynamic environment unlike the static conditions present in conventional organ models. The 3D bioarchitectures of this liver-on-a-chip device also reduce the physiological inaccuracies present in conventional organ models, allowing hepatic activity to be better modeled.

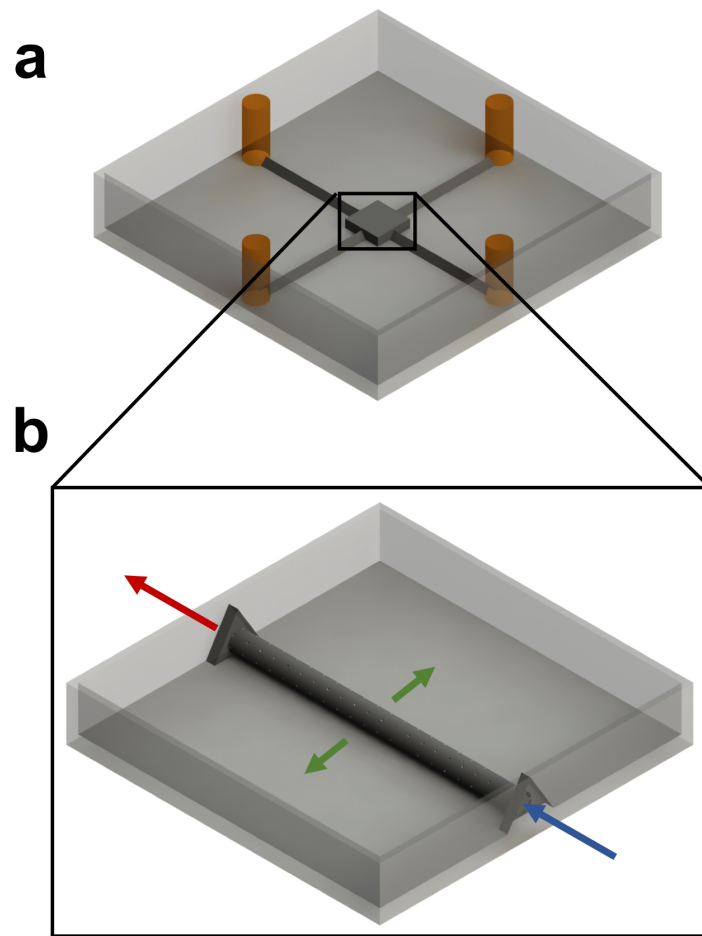


Figure 8: (a) CAD rendering of the liver-on-a-chip device design showing input and output holes for fluid flow (orange). (b) CAD rendering of cell containment chamber showing cell media input (blue), output (red), and fluid dispersion into the chamber (green).

In order to achieve this, a strategy for engineering liver sinusoids with designed fenestrae was developed using conventional microfluidic circuit theory and in-situ two photon direct laser writing (isDLW). This hybrid approach allowed for physiologically accurate fabrication of the device bioarchitectures. First, a traditional microfluidic device was designed to house the nano-3D printed bioarchitectures. Then, isDLW was used to nanofabricate a porous microchannel within the microfluidic device to represent a liver sinusoid. This microchannel was designed with inner and outer

diameters of 35 μm and 45 μm , respectively. Sets of fenestrae were also designed along the length of the microchannel with initial pore size of 0.75 μm to serve as pores allowing for the diffusion of necessary nutrients, but not cells. This design, however, showed limitations as fluid pressure decreased along the length of the microchannel, resulting in reduced fluid diffusion through the microchannel fenestrae. To create uniform flow diffusion along the length of the microchannel, fenestrae pore size was adjusted along the length of the fenestrae using circuit theory and finite element analysis (FEA) (Refer to Section 3.2).

3.2 Theoretical Methodology

One defining component of this device is its ability to sustain consistent volumetric output flow rates through the fenestrae along the entire length of the 3D printed construct. This element of the design is necessary to ensure that surrounding cells receive equal amounts of media, and therefore an equivalent nutrient supply, regardless of their location in the device. In an unoptimized fluid flow model in which the pore size is constant along the length of the construct, the output flow rate decreases linearly as fluid is lost to the surroundings and the pressure of the fluid flowing through the central tube decreases.

Circuit theory and finite element analysis (FEA) were utilized to design and validate the optimized pore design prior to fabrication. Circuit theory was applied to model fluid flow in the fenestrated tubule with the goal of calculating the pore sizes required to produce equal output flow rates

along the length of the construct. The equation that relates the voltage to the current and resistance in an electric circuit, called Ohm's Law, is shown below. For pipe flow, voltage is analogous to the pressure difference between the fluid inlet and outlet, current to the volumetric flow rate, and resistance to the resistance to fluid flow conferred by the pipe.

$$\underbrace{V}_{\text{voltage}} = \underbrace{I}_{\text{current}} \cdot \underbrace{R}_{\text{resistance}} \quad (1)$$

$$\underbrace{\Delta P}_{\text{pressure difference}} = \underbrace{Q}_{\text{volumetric flow rate}} \cdot \underbrace{R}_{\text{resistance}} \quad (2)$$

where

$$\Delta P = P_{in} - P_{out} \quad (3)$$

The fenestrated tube was modeled as a circuit in which the intermediate central tube segments and individual pores represent resistors. Placing multiple pores at the same location along the central tube allows each set of pores to be modeled as a group of resistors in parallel. The intermediate resistances conferred by the central tube act in series with each other and also with each set of pores. This model is depicted in Figure 9.

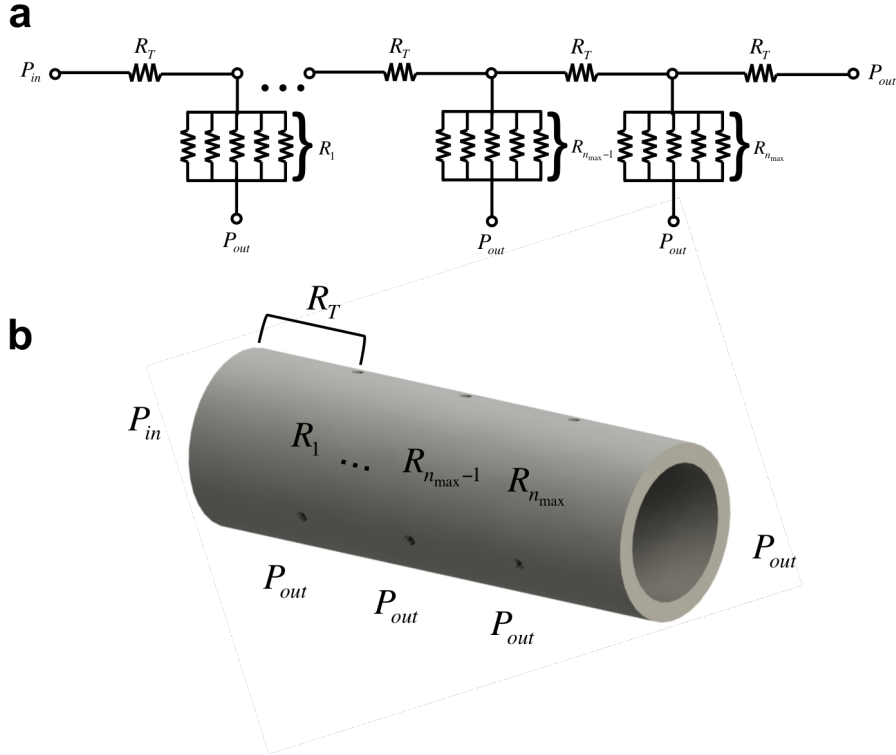


Figure 9: (a) Circuit theory model of pipe flow through a fenestrated tubule. (b) Representations of elements from circuit theory on a fenestrated tubule.

Analysis of the flow equations was conducted to evaluate the resistance of each set of pores required to maintain an equivalent output volumetric flow rate along the whole construct. There were multiple assumptions used in the creation of this model. The central tube diameter and the spacing between pores is assumed to be constant, such that the intermediate resistance R_T is constant. The distance between pores (the length used in the equation to determine the resistance R_T) is measured from the center of one set of pores to the center of the next. It was also assumed that the flow rate through the central tube must be greater than the sum of the flow rates from the pores. In this model, the resistance of the first set of pores (and therefore the radius of each pore in the first set) is treated as

an independent variable.

The equation for the resistance R_n at each pore set as a function of the pore row number (n) and maximum number of pore sets (n_{max}) was found to have the following general form:

$$R_n = (n_{max} - n + 1) \cdot \left[\left(\frac{1}{n_{max}} \right) R_1 - \left(\frac{n-1}{2} \right) R_n \right] \quad (4)$$

The general form equation is used to calculate the total resistance of each pore set. Given the number of pores in each set, the equation for equivalent resistance in parallel can be used to calculate the resistance of each pore (R_i). Finally, using the Hagen-Poiseuille equation for resistance as a function of pore length and radius, the radius of each individual pore (r) can be calculated given that the wall thickness of the tube (the length of each pore) is known.

$$\frac{1}{R_n} = \frac{n}{R_i} \quad (5)$$

$$R_i = \frac{8\eta\lambda}{\pi r^4} \quad (6)$$

It was also discovered that in order to maintain distinct pores (prevent large pores from overlapping), the intermediate resistance must abide by the following inequality:

$$R_T < \frac{2R_1}{(n_{max} - 1)(n_{max})} \quad (7)$$

As an example, for a system with 3 resistors (Fig. 10), the follow-

ing fundamental equations were outlined according to the basic pipe flow equations.

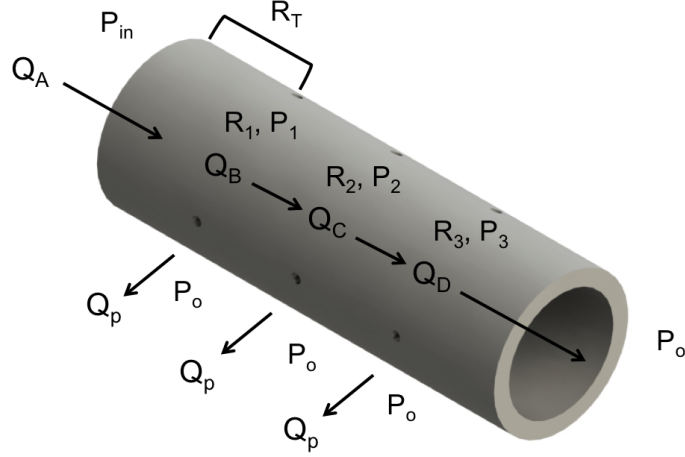


Figure 10: Circuit theory model of pipe flow through a fenestrated tubule containing three sets of pores.

$$P_{in} - P_1 = R_T \cdot Q_A \quad (8)$$

$$P_1 - P_0 = R_1 \cdot Q_P \quad (9)$$

$$P_1 - P_2 = R_T \cdot Q_B \quad (10)$$

$$P_2 - P_0 = R_2 \cdot Q_P \quad (11)$$

$$P_2 - P_3 = R_T \cdot Q_C \quad (12)$$

$$P_3 - P_0 = R_3 \cdot Q_P \quad (13)$$

$$P_3 - P_0 = R_T \cdot Q_D \quad (14)$$

$$Q_A = Q_B + Q_P \quad (15)$$

$$Q_B = Q_C + Q_P \quad (16)$$

$$Q_C = Q_D + Q_P \quad (17)$$

$$R_C = R_T + \frac{R_T \cdot R_3}{R_T + R_3} \quad (18)$$

$$R_B = R_T + \frac{R_C \cdot R_2}{R_C + R_2} \quad (19)$$

$$R_A = R_{Total} = R_T + \frac{R_B \cdot R_1}{R_B + R_1} \quad (20)$$

$$P_2 - P_0 = Q_C \cdot R_C \quad (21)$$

Equations 9 and 10 were combined to yield an expression for Q_D in terms of Q_P :

$$Q_D = \frac{R_3}{R_T} \cdot Q_P \quad (22)$$

which was substituted into equation 13 for Q_C :

$$Q_C = Q_P \cdot \left(\frac{R_3}{R_T} + 1 \right) \quad (23)$$

By substituting the right-hand side of equation 4 for the right-hand side of equation 17 and simplifying, the following expression was obtained for R_2 :

$$R_2 \cdot Q_P = R_C \cdot Q_P \cdot \left(\frac{R_3}{R_T} + 1 \right) \quad (24)$$

Further substitution with equation 11 for R_C and simplification resulted in the following expression for R_3 :

$$R_3 = \frac{R_2 - R_T}{2} \quad (25)$$

In a similar manner and by substituting in the previous equation for R_3 , the following expression was obtained for R_2 :

$$R_2 = \frac{2}{3}R_1 - R_T \quad (26)$$

The equation for R_2 agrees with the derived equation for the general form.

Using these equations, a MATLAB program was created such that the user can specify the following values (input) and obtain an output vector containing the radius of each pore, with the index in the vector corresponding to the pore row number n . These values were used to design the pore sizes in the optimized construct. The program also returns the flow rate through the first intermediate segment, $Q(1)$, which is used as the input flow rate later on in finite element analysis (FEA) to validate the design.

Inputs
Desired volumetric flow rate through each set of pores
Intermediate tube length (length between pore centers)
Center tube inner radius
Center tube wall thickness
Radius of each pore in the first set
Number of pores per set
Number of pore sets

Table 1: Custom MATLAB program inputs used for design of an optimized microfluidic tubule.

Outputs
Radii of individual pores in each of n_{max} pore sets
Flow rate through first central tube segment

Table 2: Custom MATLAB program outputs used for design of an optimized microfluidic tubule.

To determine the effectiveness of the mathematical model, output vol-

umetric flow rates in a tube with modified pore sizes as described above (optimized) and a tube with uniform pore sizes (unoptimized) were compared using finite element analysis (FEA). All simulations were performed using COMSOL Multiphysics v5.3a (COMSOL Inc., Sweden). 3D CAD models of each tube were created in SolidWorks according to the calculated dimensions and imported into COMSOL. Briefly, each pore surface was selected as an open boundary, while the appropriate ends of the central tube were selected as an inlet and outlet, respectively. Hydrodynamics equations corresponding to creeping flow were solved using these conditions, with all other boundaries set to no-slip conditions. The flow rate of the one dimensional flow field directed normally to the inlet surface was set to a velocity (m/s) corresponding to $Q(1)$, which is the calculated flow rate through the first intermediate section of the tube prior to any encounters with the pores. Water at 37 °C was selected as the input fluid for all simulations, and a normal mesh was created. A stationary study for steady state flow was then conducted, and the volumetric flow rate at each open boundary was recorded after running the simulation.

3.3 Fabrication Methodology

Our devices were fabricated using a combination of standard soft lithography and direct laser writing techniques (Fig. 11). First, a negative mold was printed and molded with polydimethylsiloxane (PDMS). PDMS was used as it is an inexpensive polymer with rubbery mechanical properties. Furthermore, the gas permeability of PDMS allows for the culture of live

cells without additional gas exchange mechanisms [48]. This micromolded PDMS was then hole punched and bonded to a glass substrate. Hollow microarchitectures with fenestrations were printed in the channels in order to house cells and distribute media or fluid in a physiologically relevant environment.

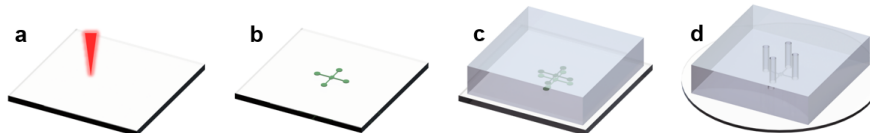


Figure 11: Device fabrication process. (a) Direct laser writing of the mold on a silicon wafer. (b) Printed mold on a silicon wafer. (c) Polydimethylsiloxane (PDMS) cured on the mold. (d) PDMS taken off the mold and bonded to a glass slide.

3.4 Microfluidic Device Manufacturing

3.4.1 Negative Mold Manufacturing

The 3D CAD model of the mold was created using through the computer-aided design software SolidWorks (Dassault Systemes, France). A negative mold was printed with a Nanoscribe Professional Photonic GT (Nanoscribe) printer on a silicon wafer. The mold was designed such that input and output ports could be created for fluid and cell flow. The mold was structured with two input and two output channels structured with triangular cross sections $50 \mu\text{m}$ in height to prevent deformation observed during iterations of the fabrication process (Fig. 11a-11b). One input and one output channel in line with each other are fabricated for the purpose of inputting and outputting the majority of fluid flow. The other input and output channels allow for cell inputs around the printed isDLW fabricated

channel. At the intersection of the four channels there is a box $100\ \mu\text{m}$ tall and $250\ \mu\text{m}$ by $250\ \mu\text{m}$ wide, for the purpose of allowing observation of cell interactions surrounding the isDLW fabricated channel. The silicon wafers were cleaned with a wash of acetone and isopropyl alcohol (IPA), and then dried with inert nitrogen gas. The Nanoscribe was used with a 25x objective lens in DiLL mode to print the molds comprised of the negative-tone photoresist, IP-S (Nanoscribe), onto the silicon wafer print substrates. The channel molds were fabricated with layer heights of $1\ \mu\text{m}$ and hatching distances of $1\ \mu\text{m}$. For DLW, the laser power and scan speed were set to 50 mW and 100 mm/s, respectively. The writing time for the negative molds was 20 minutes.

Following the DLW process, substrates were developed first in a bath of propylene glycol monomethyl ether acetate (PGMEA) for 20 minutes to remove any uncured photoresist, and then in IPA for 5 minutes so the remaining liquid could next be evaporated at $70\ ^\circ\text{C}$ for 5 minutes resulting in the desired, ready to use, negative mold.

3.4.2 Micromolding

A 10:1 ratio of elastomer base to curing agent was mixed to prepare the PDMS (Sylgard, Corning, New York). After using a dessicator to remove the excess air bubbles in the mixture, the PDMS was poured over the mold. The wafer with PDMS was put into the desiccator again to remove any additional air bubbles, and then cured overnight at room temperature or for 3 hours at $60\ ^\circ\text{C}$ on the hotplate. The structure was further refined

to remove excess PDMS, leaving a square shaped device. Holes with a diameter of 0.75 mm were created in the device at the ends of the imprinted cross pattern to create input and output valves that would interface with the microchannels.

3.4.3 Glass Bonding

In order to seal the channels, the devices were bonded to a circular glass slide with diameter of 30 mm. The devices were cleaned with Isopropyl alcohol (IPA) and dried with inert nitrogen gas prior to bonding. The glass slides were cleaned with acetone, followed by IPA, dried with inert nitrogen gas, then placed on a 120 °C hot plate to dry off completely. The device and glass were placed in the Branson Barrel Resist Stripper (Branson/IPC, New York) with the pattern on the device facing up. The power of the machine was set to 150 W with the oxygen plasma on for 45 seconds. The device and glass were then removed and the device was pressed onto the glass with the patterned side facing the glass. The bonded device was placed on a 120 °C hot plate for 10-20 minutes to ensure a tight seal.

3.4.4 Sol-Gel Coating

To minimize substrate adsorption by the PDMS device, sol gel was run through the microfluidic device channels to coat the channels with a layer of APTES. (Fig. 12) [7]. A solution of 33% APTES in EtOH was run into the device channels for 5 minutes to allow the APTES to diffuse onto the surface of the device channels. This solution was cleared with air pressure

and a 33% acetic acid (AcOH) catalyst was perfused into the channel for 3 minutes. The device was then placed on a hot plate at 90 °C for 4 minutes to evaporate the solution. This process was included in the processing of these devices as it has been shown to minimize detachment of internal 3D printed structures [7].

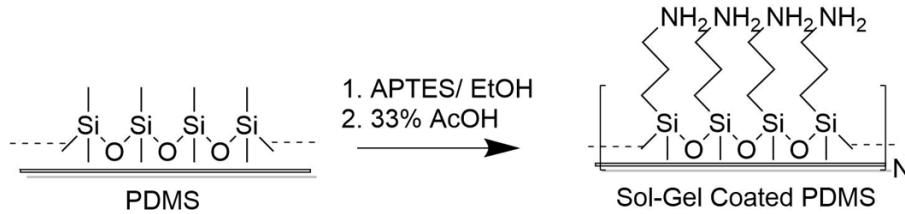


Figure 12: Sol-gel coating of PDMS with 3-aminopropyltriethoxysilane (APTES) [7].

3.4.5 Vacuum Loading of Photoresist

The sol-gel coated PDMS on glass devices were then vacuum loaded with a negative-tone photoresist to prepare for printing of the tubules. Tape was placed over two of the ports to create a seal, and the device was placed under a vacuum for 10 minutes. Photoresist was applied on top of the two open ports and allowed to flow into the channels for 5 minutes. The tape was then removed.

3.4.6 Microarchitecture Fabrication

The Nanoscribe PPGT was used again to print hollow microchannels with defined inner and outer diameters and containing patterned pores and in order to replicate the fenestrated endothelium architecture. Through the use of piezo-actuators that allow for ultra-fine guiding of the laser, micro-architectures can be precisely photocured from the material of choice.

In addition, the DeScribe (Nanoscribe, Stutensee, Germany) software associated with the Nanoscribe is compatible with .stl files generated from SolidWorks allowing for CAD designs to undergo post-processing to be suitable the NanoWrite software that directs the Nanoscribe. The microarchitectures developed for three separate devices used the Nanoscribe PPGT to print various hollow microchannels. One device featured a solid tube microarchitecture, while another featured evenly sized pores in the microchannel and the last featured a computationally determined set of variable pore size in the microarchitecture to have even fluid distribution throughout the device. The channel lengths all equaled $510\ \mu\text{m}$, with additional triangular walls $20\ \mu\text{m}$ thick to create a sealed fluidic connection from the triangular channels to the central square environment.

The Nanoscribe was used to fabricate the microchannels with a 63x objective lens in DiLL mode to print the molds comprised of the negative-tone photoresist, IP-L 780 (Nanoscribe, Stutensee, Germany), onto $107\ \mu\text{m}$ thick glass print substrates. The microchannels were fabricated with layer heights of $0.3\ \mu\text{m}$ and hatching distances of $0.3\ \mu\text{m}$. For DLW, the laser power and scan speed were set to 22.5 mW and 10 mm/s, respectively. The writing time for the microchannels was 12 minutes. Following the DLW process, substrates were developed first in a bath of propylene glycol monomethyl ether acetate (PGMEA) for 24 hours to remove any uncured photoresist. Devices were then placed for 5 minutes on heat so the remaining liquid could be evaporated at $100\ ^\circ\text{C}$.

3.4.7 Scanning Electron Microscopy

Scanning electron microscopy (SEM) images of samples were taken with Field Emission Gun Scanning Electron Microscopy (FEGSEM) operating at 10.0 kV. Samples were first mounted on an aluminum stub and then carbon sputtered (Balzers MED 010 Carbon Coater) with a thickness of roughly 10 nm before analysis with SEM (Tescan XEIA3 FIB/SEM).

3.5 Fluid Flow Testing

3.5.1 Flow Visualization in 3D Printed Tubules

In order to control fluid flow, a pressure control system was used. This system utilized a pressure regulator device to control the pressure applied to a fluid. The device system that was used was designed specifically for organ-on-a-chip systems, as it includes the capacity control to critical parameters such as flow induced shear stress, mechanical simulation, and air-liquid interface [49]. The specific system that was used is the Fluigent MFCS™-EZ system, shown in Figure 13. The MFCS-EZ has 4 channels that can be controlled on the computer using MAESFLO software, also shown in Figure 13. This software can regulate the pressure of the fluid flowing through each channel [50]. In addition, Fluigent flow sensors were used in conjunction with the MFCS-EZ system as a means of measuring the speed of the fluid flow [51]. Autofluorescent polymer-based particles with a diameter of 300 nm (Thermo Scientific, Massachusetts) were dissolved in a 1:1000 dilution by volume in water. This solution was pumped through

the channels to observe the fluid flow out of the pores of the microtubule in the device using the Axiocam 503 Mono Microscope (Zeiss, Germany) at 18 mbar [7].

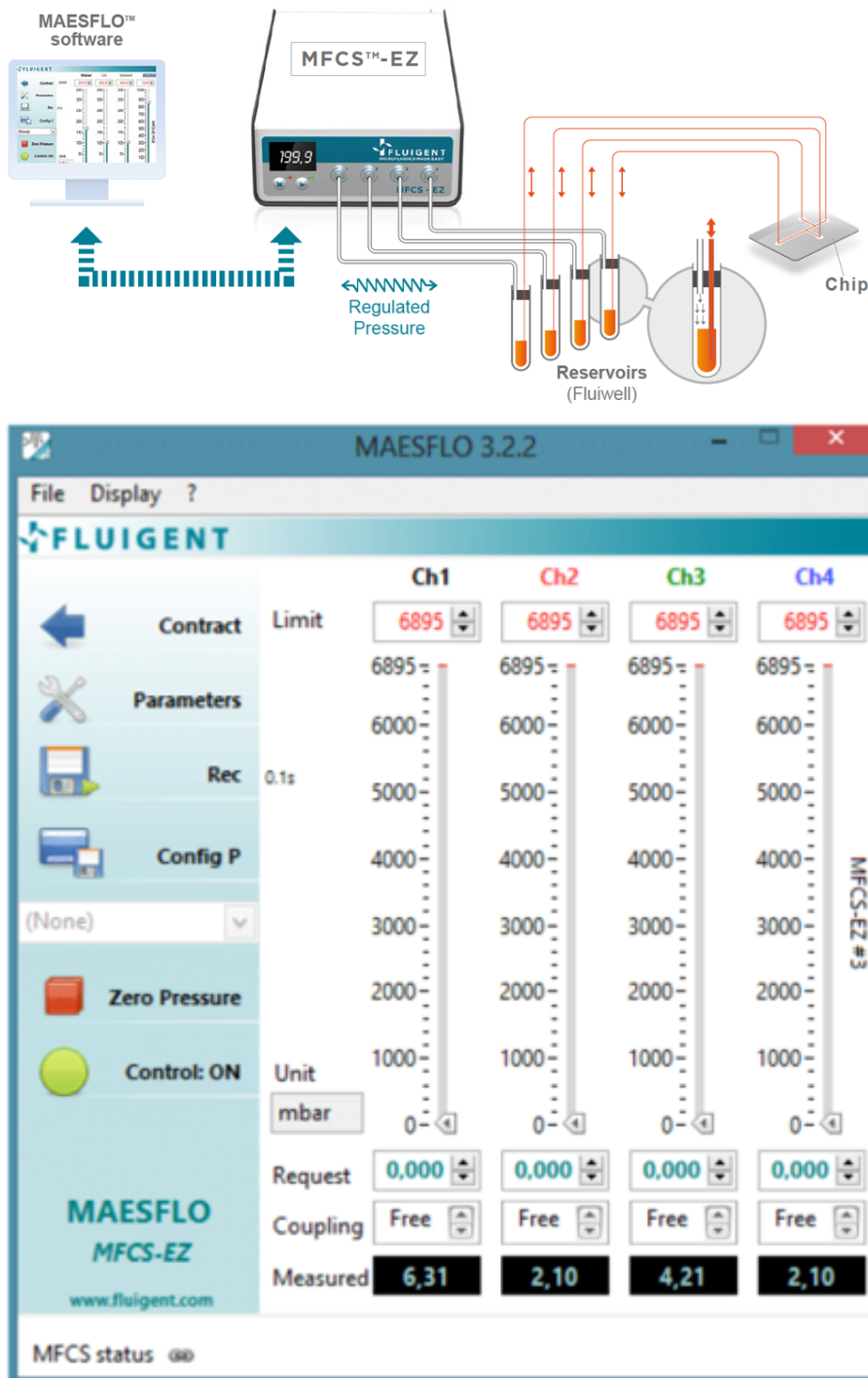


Figure 13: Fluigent MFCS-EZ system and Maesflo software used for fluid flow testing [50].

3.5.2 Leakage Test

A leakage test was conducted to determine if there was an intact seal between the 3D printed structures and the walls of the microchannel. A microfluidic device was formed using an H-shaped negative mold. Next, a semicircle-shaped barrier was printed using the Nanoscribe in the central portion between the two parallel channels of the device. Using the Fluigent system, pressurized water was inputted through one of the channels at incrementally increasing pressure until the fluid burst through the printed wall to the other channel of the device.

4 Results

4.1 Theoretical Results

The fenestrated tubule design was created using the derived equation for resistance as a function of pore row number (general form), the derived inequality governing restrictions on pore size, the Hagen-Poiseuille equation for resistance, and the equation for resistance in parallel that is governed by hydraulic circuit theory.

For theoretical studies, tubules with the following dimensions were fabricated in SolidWorks.

Parameter	Value
Inner diameter	35 μm
Wall thickness	5 μm
Pore row number	50
Number of pores per set	5
Radius of first pore	0.75 μm
Spacing between centers of pore rows	10 μm

Table 3: User-specified parameters for design of an optimized microfluidic tubule.

The value for the inner diameter was selected to reflect the diameter of a large sinusoid without the presence of endothelial cells. This is because our initial intention was to culture a thin layer of endothelial cells within the 3D printed channels, therefore necessitating a larger tubule diameter. While typical liver sinusoid diameters range in size from 7-15 μm , the vascular endothelial cells that line the inner wall have diameters of around 6.5 μm [52]. Therefore, the expected diameter of a large sinusoid without

the endothelial cells would be: $15+2(6.5)=28 \mu\text{m}$. Our model includes some extra space for replicability, with an inner diameter of $35 \mu\text{m}$. A wall thickness of $5 \mu\text{m}$ was chosen because it is similar to the diameter of an endothelial cell. This is significant because the sinusoid walls are themselves composed of endothelial cells with a thin basement membrane. In addition, this size could be reliably printed without collapsing. A tubule length of $510 \mu\text{m}$ was chosen because it represents the length of a sinusoid within a typical liver lobule. Lobules are generally around 1 mm in diameter, with sinusoids branching in from the exterior to the portal vein in the center [53]. Therefore, the distance to the portal vein is around $500 \mu\text{m}$.

The spacing between the centers of each pore row, and deductively the number of pore rows, was chosen such that a nontrivial increase in pore size could be observed without breaching the governing inequality of the model. The number of pores per set was also chosen according to this reasoning. For the non-optimized design, the radius of each pore was set to $0.75 \mu\text{m}$. For the optimized design, the radii of the pores in the first set only were designated as $0.75 \mu\text{m}$. The radii of the pores in each of the subsequent sets were calculated using the custom MATLAB program. Figure 14 shows the pore radii for each of the 50 pore rows in the optimized design.

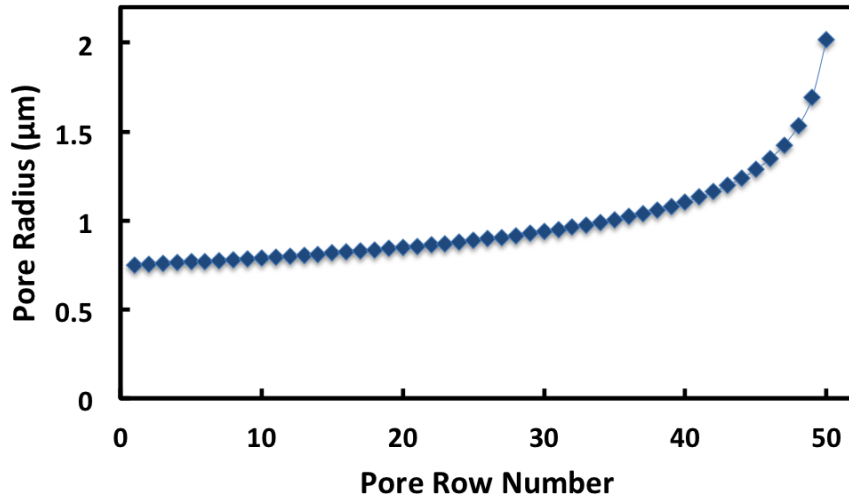


Figure 14: Pore radius as a function of pore row number in the optimized tubule. Each row contains five individual pores.

The CAD designs of each of the tubules are shown in Figure 15.



Figure 15: (a) CAD rendering of the unoptimized tubule design with consistent pore radii. (b) CAD rendering of the optimized tubule design with variable pore radii.

The desired output volumetric flow rate through each set of pores was selected such that the input volumetric flow rate $Q(1)$ corresponded to an input velocity of 0.5 mm/s, which is the approximate blood flow rate through the sinusoids. The viscosity of water at 37 °C was chosen as a representative for blood in the Newtonian model. The values of the input parameters relating to fluid flow for the custom MATLAB program are shown below.

Parameter	Value
Flow rate through each set of pores	$7.78 \cdot 10^{-16} \text{ m}^3/\text{s}$
Fluid viscosity	$6.922 \cdot 10^{-4} \text{ Pa}$

Table 4: User-specified values of input parameters related to fluid flow.

Results displaying the output volumetric flow rates computed by COMSOL for the unoptimized and optimized designs are shown in Figure 16.

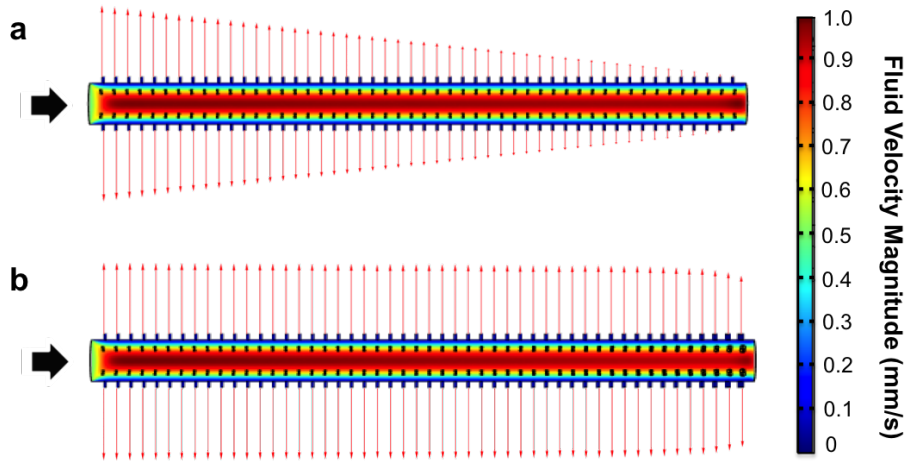


Figure 16: Fluid velocity magnitude plots generated in COMSOL for (a) unoptimized and (b) optimized tubules. Output volumetric flow rate relative to the first set of pores is represented by red arrows.

As seen in Figure 16a, the flow rate in an unoptimized design decreases significantly relative to the first pore, with almost no flow at the 50th and final set of pores. In the optimized design, flow appears to be steadily maintained until around the 42nd set of pores, where it decreases marginally. A quantitative representation of these results is shown in Figure 16b.

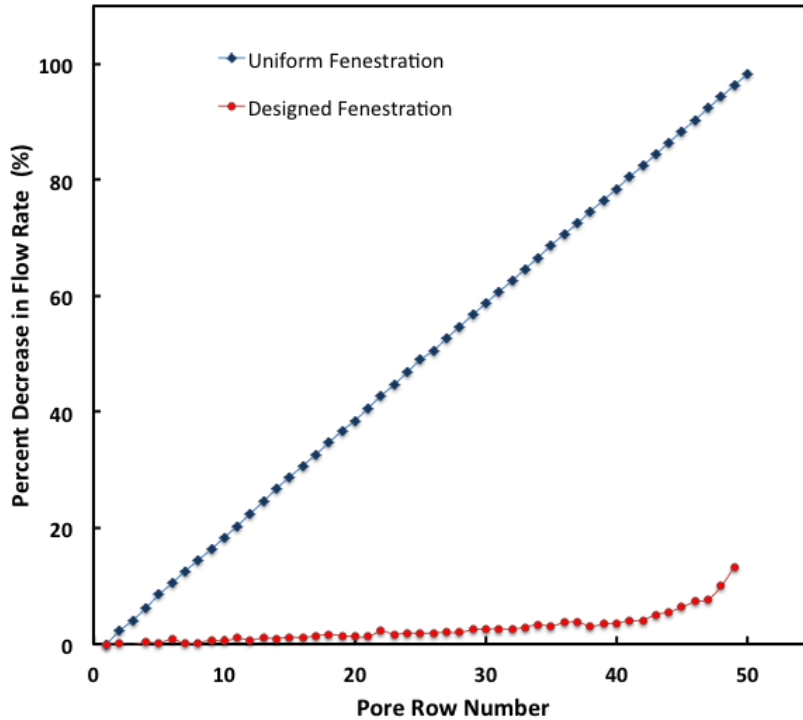


Figure 17: Percent decrease in volumetric output flow rate as a function of pore row number in tubules with uniform and designed (modified) fenestration.

The percent decrease in flow rate relative to the first pore, described in Figure 17, increases linearly for the unoptimized design, with a nearly 100% decrease at the final set of pores. In contrast, the optimized design produces a negligible change in flow rate in the first half of the tubule (up to around pore number 25), followed by a marginal (4%) decrease by the 40th row and finally an ultimate decrease of around 18% by the final pore row.

4.2 Device Fabrication

Fabrication of the microfluidic devices begins with the clear and viscous PDMS elastomer and curing agent mixture, as described in Figure 18. Figure 18a shows the initial materials which are generally clear and viscous

with very few bubbles. These materials are thoroughly mixed to fully blend in the curing agent, through which air is incorporated into the mixture. To eliminate these air pockets, the mixture is placed in a desiccator, leaving the mixture looking more opaque and frothy in texture. Desiccation continues until the mixture is completely clear, and all bubbles are eliminated. This clear mixture is then poured on to the inverse molds, as seen in Figure 18b, and allowed to cure on gentle heat. Figure 18c shows the hardened PDMS once cured and is no longer malleable to a shape. If manipulated these devices exhibit elastic properties. Post processing steps include cutting the device to fit the glass slide and creating fluid flow channels from the top of the device to the microchannel. The final devices vary in height but are approximately a centimeter tall. Then these devices were plasma-bonded to glass slides with a diameter of 30 mm.

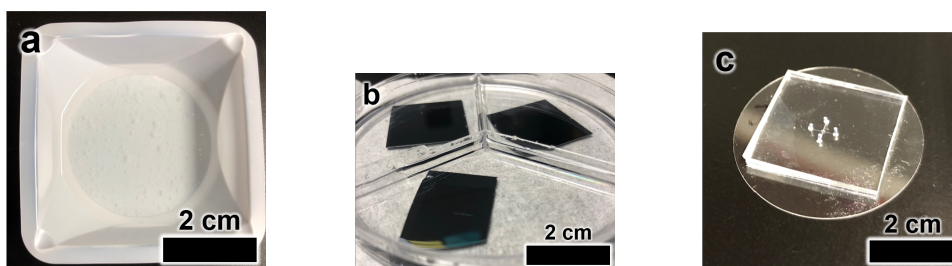


Figure 18: Microfluidic device fabrication. (a) PDMS mixture prior to curing. (b) Cured PDMS on inverse molds. (c) Device prior to printing.

The microchannels prior to the internal sol-gel coating, shown in Figure 19a, have a pure PDMS border. After the sol-gel coating, the devices exhibit a dark border along the edges of the microchannel, shown in Figure 19b. Finally, the fully fabricated devices, shown in figure 18c, are prepared for printing.

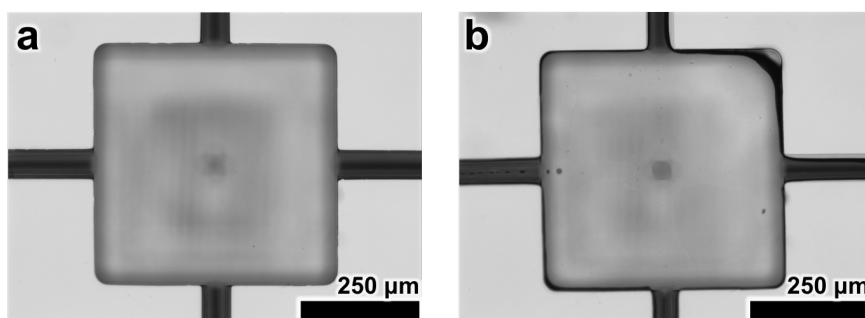


Figure 19: Central chamber of the microfluidic device (a) before, and (b) after sol-gel coating. The sol-gel coating is visible as a thin black border on the walls of the chamber.

4.3 Proof of Concept Studies

Initial proof of concept testing involved fabrication of tubules from two candidate materials, IP-L 780 and OrmoComp. IP-L 780 is a liquid photoresist that has been used to produce the highest resolution prints on the Nanoscribe to date [54]. However, it is autofluorescent, which may pose challenges for fluorescent imaging or assay studies. OrmoComp is a glass-like material with a high thermal and mechanical stability that has proven to be non-cytotoxic in multiple studies [55, 56]. OrmoComp was initially identified as the photoresist of choice for this project due to its material properties and its biocompatibility. However, this material produced prints with compromised structural integrity, a lack of agreement to the print file, and inconsistency between print tests. Figure 20a shows the design for a solid tubule that was printed with OrmoComp. The inconsistencies of print results observed amongst identical print parameters are shown in Figure 20b and Figure 20c.

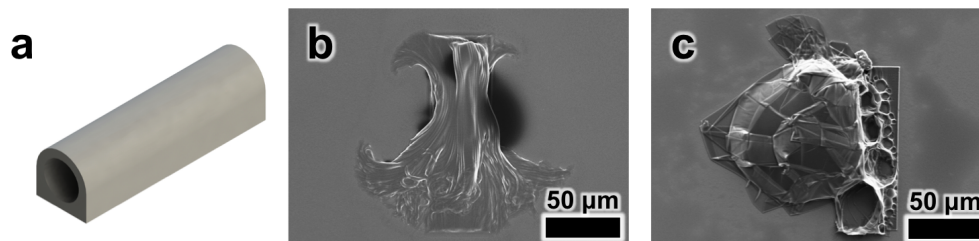


Figure 20: Printing studies with OrmoComp. (a) CAD rendering of the solid tubule design. The design features a rectangular base to ensure that the tubule is supported on the glass slide. Previous prints without this modification failed to attach. (b) Deformed OrmoComp tubule on a glass slide. (c) Burned OrmoComp tubule on a glass slide.

In both cases, the structure was highly deformed and unrepresentative of the designed tubule. In Figure 20c, this was due to burning of the material. Burning was visible during multiple prints as dark “bubbles” that emerged rapidly and compromised the laser’s ability to further cure the photoresist. The print job was aborted after the observation of burning.

Despite multiple attempts to adjust the printing parameters and file properties, OrmoComp could not be reproducibly or reliably printed, whether due to structural deformation or burning. On the other hand, IP-L 780 structures could be consistently reproduced and demonstrated agreement between the CAD file and print outcomes. Figure 21 shows the design and print results of a fenestrated IP-L 780 tubule that was printed on a glass slide. The design in Figure 21a features multiple sets of equally sized pores that permeate the wall of the tubule.

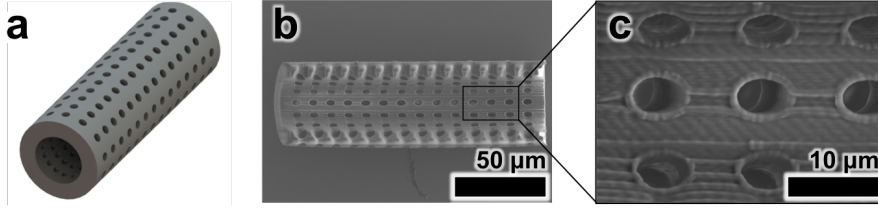


Figure 21: Printing studies with IP-L 780. (a) CAD rendering of the fenestrated tubule design. (b) SEM image of the printed tubule on a glass slide. (c) SEM image of pores.

The agreement of the print with the CAD file is evident upon inspection of Figure 21b. The resolution of the print is further demonstrated by the contour and hatching lines visible around the pores in Figure 21c. In addition, the pores have a consistent size and spacing. Based upon these results, IP-L 780 was selected as the printing material for the remainder of the project.

4.4 Barrier Tests

A microfluidic device consisting of two parallel channels connected in the center by a short intermediate channel was created for pressure testing (Fig. 22a). This device is designed such that the central connecting channel can house a printed barrier that separates the parallel channels. The purpose of this experiment was to apply fluid flow in the parallel channels to confirm the integrity of the seal between the printed structure and the walls of the device. The open central channel prior to printing is shown in Figure 22a. A semicircle-shaped barrier according to the dimensions shown in Figure 22c was printed inside the channels. The result of the print is shown in Figure 22b.

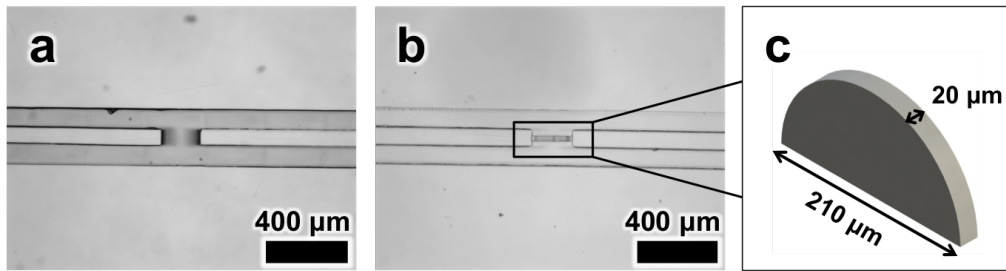


Figure 22: H-shaped microfluidic device showing (a) the sol-gel coating prior to printing, and (b) the 3D printed barrier. (c) CAD rendering of the semicircle-shaped 3D printed barrier.

Upon visual inspection, the barrier appears to be aligned in the center and in contact with both sides of the channel. This observation was confirmed by applying fluid flow to one of the channels. Figure 23 shows the initial application of the flow. The pressure was progressively increased, at which point the seal was compromised and fluid flowed rapidly out of the channel. No fluid flowed across the barrier prior to bursting, indicating that there was a complete seal with the wall preventing leakage.

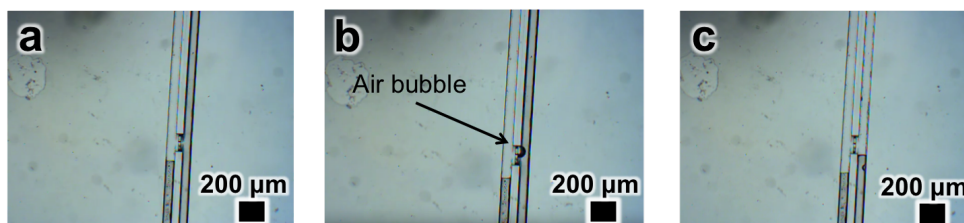


Figure 23: Results from the application of fluid to one of the parallel channels. (a) Demonstrated integrity of the barrier under low pressure conditions. (b) Bursting of the barrier as the pressure was increased. (c) Outcome immediately after bursting. Fluid flowed rapidly out of the channel.

4.5 Solid Tubules

For prints containing solid tubules, a cross-shaped microfluidic device consisting of two perpendicular channels was created (Fig. 25). This design enabled the tubules to be sealed to either end of the channels and printed

across the center. The mold design featured a triangular channel structure unlike that of the H-shaped microfluidic devices. A mold containing these triangular channels was printed using IP-L 780, followed by application and curing of PDMS and bonding to a glass slide. Holes were then punched to create four outlets for flow at each end of the cross. The purpose of this experiment was to show that a tubule with the desired dimensions could be printed in a microfluidic device prior to investigating the fenestrated designs. After constructing the tubule in CAD (Fig. 24a), triangular structures with a cylindrical opening the size of the tubule inner diameter (block ends) were added to either end (Fig. 24b). These structures serve as attachment points on either end of the triangular microfluidic channels.

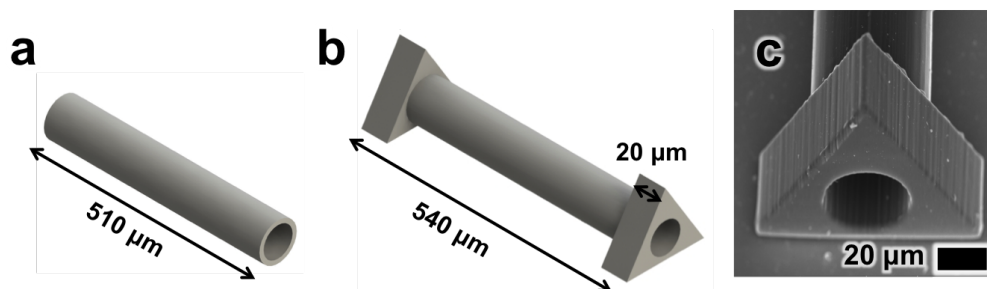


Figure 24: (a) CAD rendering of the solid tubule. (b) CAD rendering of the tubule with “block ends” for attachment to the microchannel walls. (c) SEM image of a block end connected to a solid tubule.

The inside of the microfluidic device prior to printing is shown in Figure 25a, and the result of the print is shown in Figure 25b. The tubules are printed such that they barely make contact with the bottom of the device.

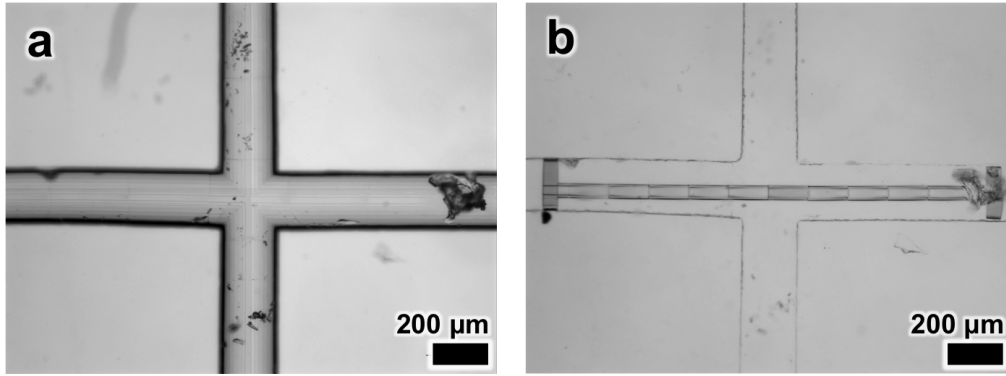


Figure 25: Cross-shaped microfluidic device showing (a) the sol gel coating prior to printing, and (b) the 3D printed tubule.

The shape present on the right side of the channel is likely dust or debris that entered the channel following the initial fabrication process, as debris was most often observed following application of the sol gel coating. However, the debris did not interfere with the print. The block ends of the printed tubule appear to make contact with the walls of the channel, although there is a slight gap on the right side. The channel has a segmented appearance.

4.6 Unoptimized and Optimized Tubules

For prints containing fenestrated tubules, a microfluidic device consisting of a square-shaped central chamber with four outlets was created. This design enabled the tubules to be sealed to either end of the channels and printed across the center. The open space in the chamber is representative of the area that would be occupied by cells in an organ-on-a-chip device. The mold design featured the same triangular channel structure as for the solid tubule prints. A mold containing these channels was printed using IP-L 780, followed by application and curing of PDMS and bonding to a glass

slide. Holes were then punched to create four outlets for flow at each outlet. After constructing the tubule in CAD (Fig. 26), triangular structures with a cylindrical opening the size of the tubule inner diameter (block ends) were added to either end. These structures serve as attachment points on either end of the triangular microfluidic channels.

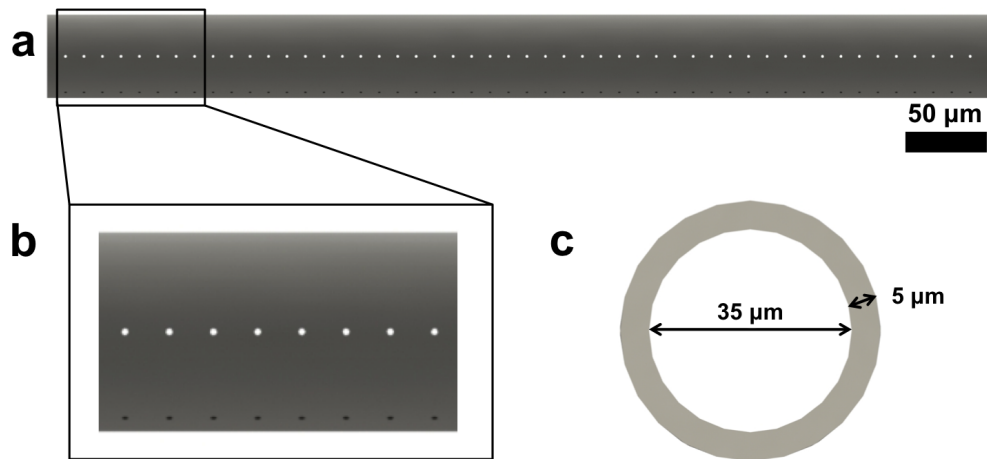


Figure 26: CAD rendering of the unoptimized tubule. (a) 510 μm long tubule. (b) Zoomed in view of pores with radii of 0.75 μm . (c) Cross section of the tubule with dimensions.

Fenestrated microchannels with a uniform pore radius of 0.75 μm were successfully printed inside the microfluidic devices. The results from this print of the unoptimized tubule are shown in Figure 27.

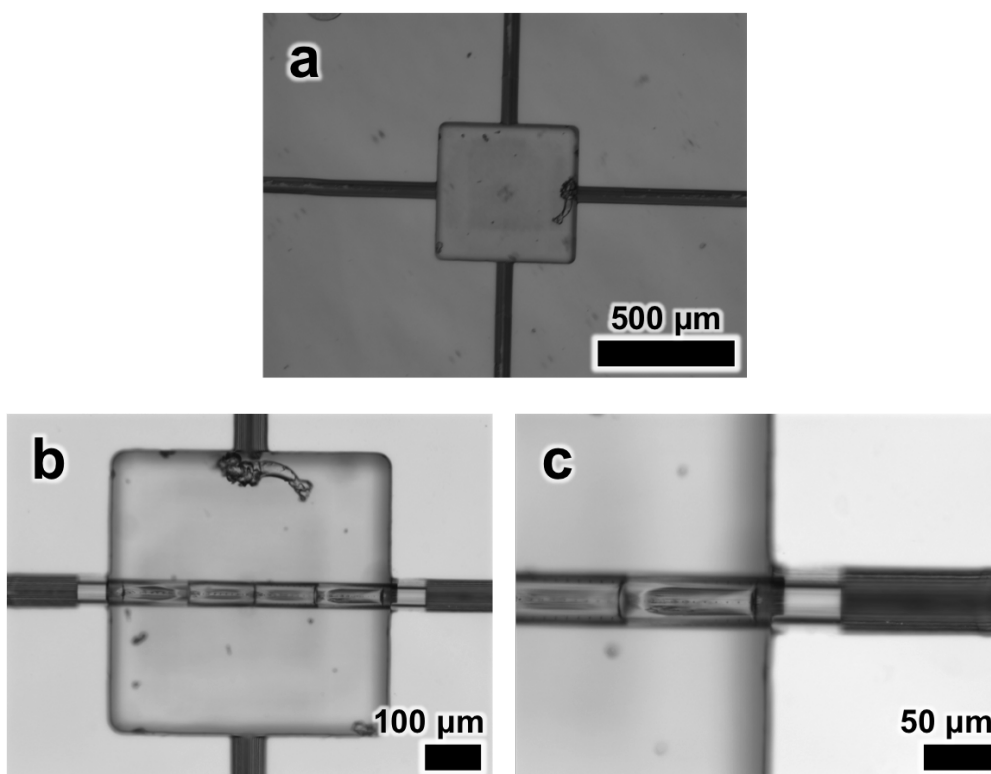


Figure 27: Unoptimized tubule inside a microfluidic device. (a) Device with sol gel coating prior to printing. (b) Device containing printed unoptimized tubule. (c) Magnified image of the seal between one block end of the unoptimized tubule and the microchannel walls.

Upon visual inspection, the unoptimized microchannel appeared to be sealed within the microfluidic chamber. Debris was present inside the device but did not interfere with the microchannel fabrication process due to its location away from the print. Distinct pores are displayed along the length of the microchannel in Figure 27b, and a sealed barrier is shown in Figure 27c.

Following the successful fabrication of an unoptimized microchannel, an optimized microchannel was fabricated using the pore radii calculated in Section 4.1.

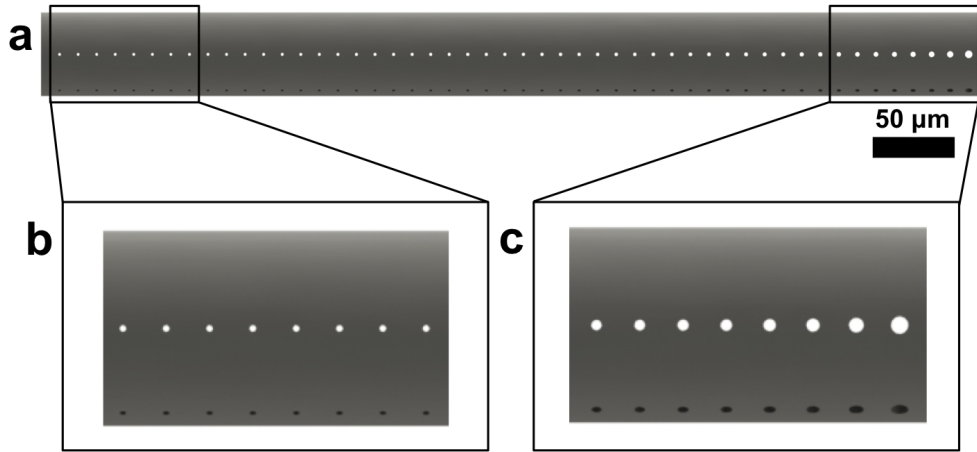


Figure 28: CAD rendering of the optimized tubule. (a) 510 μm long tubule. (b) Zoomed in view of pores in the initial section. (c) Zoomed in view of pores in the terminal section.

Fenestrated microchannels with gradually increasing pore radii were successfully printed inside the microfluidic devices. The results from this print of the optimized tubule are shown in Figure 29.

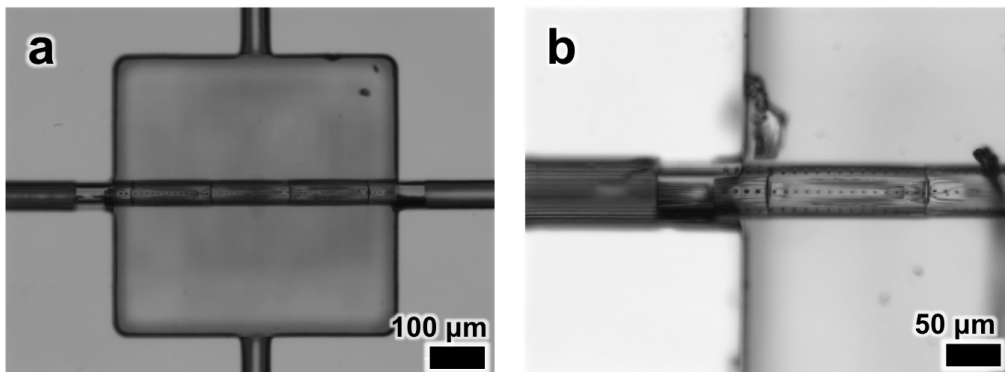


Figure 29: Optimized tubule inside a microfluidic device. (a) Device containing printed optimized tubule. (b) Magnified image of the seal between one block end of the optimized tubule and the microchannel walls.

The optimized microchannel also appeared to be sealed within the microfluidic chamber. The device appeared to contain nearly no debris, and pores are present along the length of the microchannel (Fig. 29b). Additional imaging was performed to examine the pore size distribution along the length of the optimized microchannel.

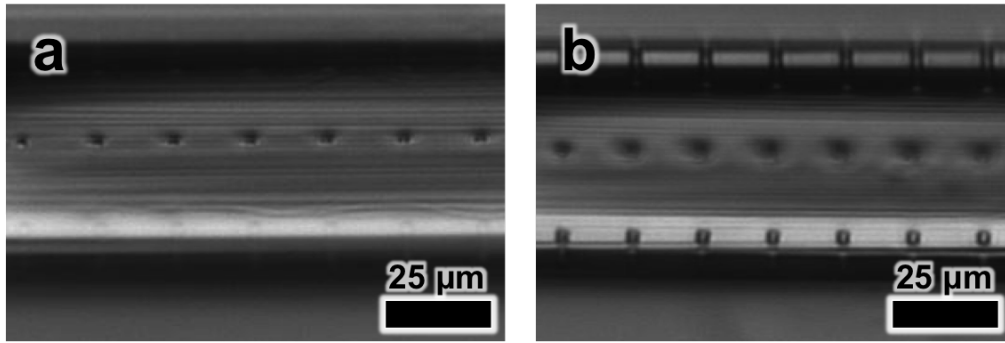


Figure 30: Zoomed in view of pores in (a) the initial segment of the optimized microchannel, and (b) the terminal segment of the optimized microchannel.

Upon visual inspection, the pore sizes at the terminal end of the optimized microchannel appear to be larger in diameter (Fig. 30).

4.7 Fluid Flow Testing

Fluid containing 300 nm autofluorescent particles was run through an optimized tubule to examine the flow distribution. This tubule was 260 μm long with 25 sets of pores ($n=25$).

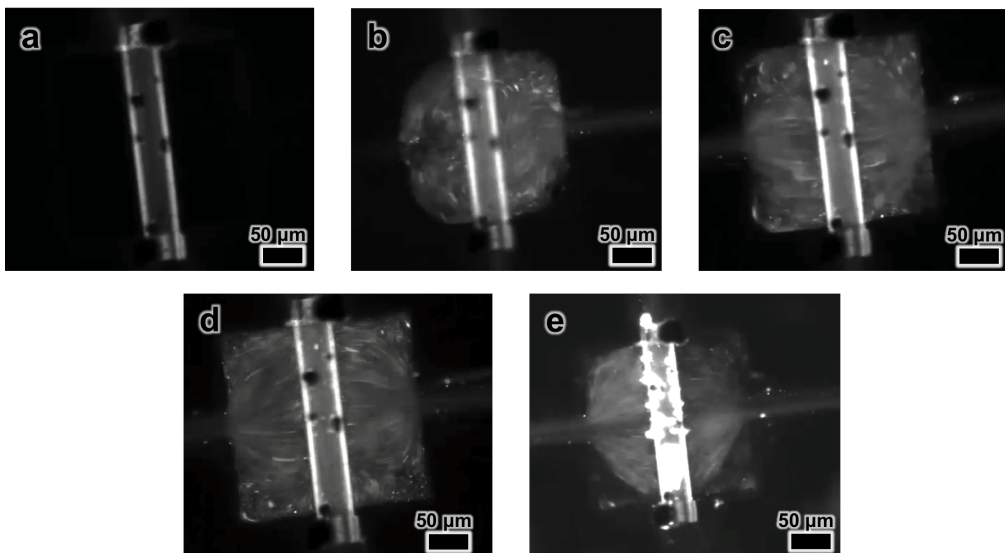


Figure 31: Fluorescence micrographs of fluid testing experimental results. (a) Tubule before application of fluid. Images taken (b) 1 second, (c) 2 seconds, (d) 3 seconds, and (e) 7 seconds after initiating fluid flow.

After inspection of fluid flow images, it was observed that fluid flow remained at a constant flow rate throughout the length of the tubule (Fig. 31). Fluid distribution began to assume even outflow by 2 seconds (Fig. 31c-d), and maintained this evenly distributed outflow along the length of the tubule even in the presence of debris (Fig. 31e).

5 Discussion

5.1 Theoretical Results

According to results obtained in COMSOL, a fluid flow model was created such that the output volumetric flow rates along the length of the construct remained relatively constant. In comparison to a near 100% decrease in flow rate at the 50th pore in the unoptimized model, the optimized model demonstrated a modest decrease of only around 18%. Despite this improvement, the model is clearly not idealized. This is likely due to the definition of the length between pore rows, which is considered from the center of one set of pores to another. The equation used to calculate R_2 based upon this length is governed by the assumption that this segment of the tube is solid. However, due to the sets of pores on either side, there is a smaller overall surface area than assumed by the equation. As the pores become larger, this effect is more significant, resulting in greater deviations from the expected flow rate. Because R_T is marginally smaller than calculated, the overall pressure in the central tube is lower than calculated, eventually leading to a measurable difference in the flow rate out from the pores.

The pores in this model were designed such that the spacing between pore rows and the diameter of the pores in each row were constant. These conditions facilitated the derivation of the general form equation and the creation of a model that maintains a consistent output volumetric flow rate. However, fenestrae *in vivo* are arranged randomly along the length of

the sinusoid and have variable diameters on the order of nanometers. Due to the complexity of creating a mathematical model for these randomly varying parameters, the effect of constant vs. random pore size (within the pore rows) and constant vs. random spacing between pore rows was not investigated. However, it may be useful to investigate the impact of this random arrangement on cell viability and metabolic activity in future models that do not rely on this constraint.

Within the scope of this project, the introduction of variable pore sizes into the model was an important consideration for maintenance of a constant output volumetric flow rate. This is because the initial goal was to culture one cell population only, primary hepatocytes, in the area surrounding the tubule. However, sinusoids *in vivo* also contain endothelial cells that compose the walls of the vessels, where the fenestrae are formed via junctions between neighboring cells. As a result, these endothelial cells play a central role in the regulation of fluid flow and nutrient exchange between the sinusoid and the surrounding environment. A more biologically complex model that contains endothelial cells would necessitate a fundamentally different tubule architecture in which the fenestrae themselves can be formed by the cells. Therefore, a tubule design for this model would have to provide a sinusoid-shaped structure for cell adhesion while maintaining sufficient open space for nutrient exchange to be unobstructed by the printed wall. Assuming the cells can assemble into a monolayer in such a model, they should be capable of replicating their *in vivo* functions by altering vascular tone in response to shear stresses under varying flow

conditions. Therefore, incorporation of pores into the 3D printed tubule would not be necessary.

5.2 Fabrication Results

Figures 20b and 20c show the two types of deformed structures that were printed using the initial material, OrmoComp. Despite many attempts, a tubule in agreement with the CAD design could not be printed due to increased resulting inconsistency as compared to alternative materials. Therefore, IP-L 780 was chosen as the material for this project.

The initial molds for the microfluidic channels were created with a semicircle shape, and this was the structure that was used to create the H-shaped molds. However, during the project it came to light that a triangular shaped microfluidic channel was beneficial for obtaining a complete seal with the walls of the channel [7]. Generally, it was discovered that outward tapering structures improved sealing performance of the 3D printed structures. It is hypothesized that this is due to a phenomenon called “shadowing” in which focusing deviations occur due to the path of the laser through certain portions of the PDMS. This prevents photocuring of some of the material in the channel, resulting in an incomplete seal. The triangular mold design used to overcome this limitation is shown in Figures 32 and 33.



Figure 32: CAD rendering of the mold used to fabricate microfluidic devices with triangular channels. The width of the central chamber is 250 μm .

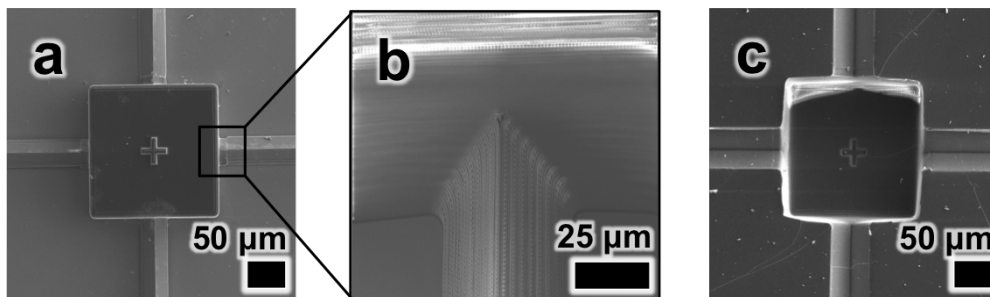


Figure 33: 3D printed mold with triangular channels. (a) SEM image of the central chamber. (b) SEM image of the triangular channel connected to the central chamber. (c) SEM image of the mold coated with PDMS.

For the initial solid tube prints, a cross shaped mold was used (Fig. 25a). For the fenestrated prints, a mold with narrower channels and an open inner chamber was created to model the space where cells would be cultured around the tubule (Fig. 27a).

The purpose of the tests conducted using the H-shaped mold was twofold. The first goal was to confirm that an IP-L 780 structure could be printed inside a tubule such that it was completely sealed to the outside walls of the channel. The fluid flow experiment demonstrated that when water flowed along one side of the channel, no liquid was visible on the other side. Therefore, no leakage occurred through the barrier, confirming the integrity of

the seal. When the pressure was increased, the structure eventually burst and the fluid on the right side was pushed out of the channel. However, it is unclear whether the seal with the wall or the structure itself was compromised. A future modification of this experiment could involve gradually increasing the pressure using the Fluigent and recording the pressure at which bursting occurs for both a semicircle-shaped barrier in semicircular channels and a triangle-shaped barrier in triangular channels.

5.3 Printing Results

The first prints were conducted with a solid tubule design to confirm that tubes could be printed inside the microchannels. In Figure 25a, which shows the channels of the microfluidic device following sol gel, there are some visible particles along the vertical direction in addition to a large piece of debris on the right side of the horizontal channel. Debris was most likely introduced during the sol gel process, by which solutions and air are pushed through the channels. Reusing tubing that was not clean or failing to push the air through at a high enough speed could introduce debris into the channels or fail to clear it out. This problem was mitigated by using new tubing and catheter couplers each time for sol gel. As seen in Figure 25b, the debris did not appear to interfere with the printing process. While the barrier on the left appears to make full contact with the walls of the channel, there is a slight gap on the bottom portion of the barrier at the right. This is likely due to a slight error when orienting the initial location for the print. In future prints this problem was able to be avoided.

The segmented appearance of the channel is due to restrictions on the Nanoscribe print area as a result of the working distance of the print laser, which is around $350\ \mu\text{m}$. With the addition of the glass print substrate, the maximum print length that can be achieved without moving the print substrate is about $250\ \mu\text{m}$. As a result, the printer must move the stage to print constructs that are longer than approximately $250\ \mu\text{m}$. The visible segments in the channel show the starting point of the print after moving the stage.

5.4 Experimental Verification of Designed Fenestrae

Fluid flow testing yielded results showing near uniform fluid flow rates throughout the length of the tubule. While the tubule was burned during the printing process, it appears that the burns were minor and had no effect on fluid flow through the fenestrae of the tubule. Furthermore, it can be seen that fluid flow through the tubule remained uniform even in the presence of debris. Experimental fluid flow observations of the optimized tubule correlate with theoretical calculated results of equal output volumetric flow rates generated in COMSOL. Thus, the engineered micro-tubule with fenestrae yields near-uniform flow rates along the length of the tube which correlates both theoretical and experimental work.

A tubule with a length of $260\ \mu\text{m}$ was used for fluid testing as opposed to the $510\ \mu\text{m}$ long tubule investigated in the theoretical studies. This is because the Nanoscribe must move the stage to print the longer tubule, resulting in visible creases where the tubule is stitched together. Initial

fluid flow testing showed that tubules burst at the location of stitching (data not shown). Therefore, only tubules that meet the constraints of the Nanoscribe print area can feasibly be utilized for fluid flow. For the fluid flow testing, a construct with a total length of 290 μm including the block ends was successfully printed without moving the stage.

5.5 Future Work

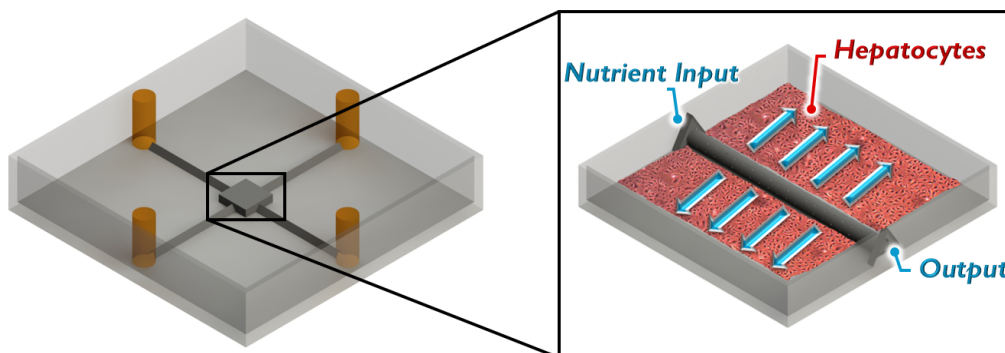


Figure 34: CAD representation of a cell-seeded chamber with a central fenestrated tubule for diffusion of vital nutrients.

Following successful fluid flow through the optimized tubule, the device would be able to evenly distribute media to surrounding cultured cells to resemble the physiological conditions of the liver (Fig. 34). The effects of the device could be ascertained by culturing hepatocytes in the open chamber and observing the cell viability and metabolic function. A hepatic cell line that could be used is Huh-7.5. Huh-7.5 cells produce albumin and have the same drug metabolism as primary hepatocytes, along with being permissive to hepatitis C infection. They are widely used because of their ease of growth and cultured in a media with Dimethyl Sulfoxide [57]. Cell viability could be observed using a live/dead assay. These kits deter-

mine the cell viability through the cell staining method, which marks living cells with green fluorescent dyes and dead cells red fluorescent dyes [58]. To further resemble the environment of the human liver, endothelial cells could be seeded in the interior of the microchannels. This would mimic the endothelial cells that compose the fenestrated liver sinusoid. Albumin, an essential protein made in the liver, is vital in maintaining oncotic pressure and transporting hormones and various drugs. Measuring the presence and relative amounts of albumin is one of the standard liver function tests. The metabolic activity of the hepatocytes could further be evaluated by observing albumin production through an enzyme-linked immunosorbent assay (ELISA) [59, 60]. Cytochrome P450 enzymes are also responsible for metabolizing drugs, and thereby their levels are indicative of hepatic metabolic function. These can be analyzed through quantification of immunofluorescence microscopy through ImageJ using anti-CYP450 primary antibodies (Abcam) and a secondary fluorescent antibody [61].

Another future direction involves the incorporation of multiple 3D printed tubules into a single microfluidic chamber. Liver sinusoids *in vivo* have a spacing of about $x \mu\text{m}$, which enables adequate dispersion of nutrients to all surrounding hepatocytes. In order to replicate this architecture and prevent cell death due to inadequate proximity to the sinusoid, multiple tubules could be printed in a larger chamber with a spacing of about $x \mu\text{m}$. The inner diameter of the tubule is $35 \mu\text{m}$, thus, given that liver endothelial cells are $6.5 \mu\text{m}$ in diameter [52], it is anticipated that fluid flow will pass through the tubule of the device. Furthermore, we would anticipate that a

gradient away from the tubule would exist for fluid and thus nutrient flow should cells be seeded in this device.

This device that resembles the physiological environment of the human liver would have many further applications. It could be used in the early stages of drug testing to provide more accurate predictions of the interactions between the drug and cells than traditional 2D cell culture methods. For initial testing, one relevant drug that could be tested is acetaminophen, which is known to be a cause of liver damage and failure in certain doses. The model can also be applied to study the effects of alcohol on the liver. As the body is exposed to alcohol, the liver produces a number of toxic substances including acetaldehydes and highly reactive molecules called free radicals. These can induce further liver damage and disease [62]. By exposing the liver cells in our model to alcohol, this process could be observed and analyzed more effectively than previous traditional methods of cell cultures in petri dishes. Through these experiments, our model could be utilized for further research on the liver and liver diseases.

Our liver model could also be used to study viral-host interactions and other interactions with the liver in a more physiologically accurate manner. If our model induces greater cell differentiation, it is possible that our liver on a chip device may result in better hepatocyte expression of liver specific factors, which could enable greater permissibility of infectivity and longevity of primary hepatocytes if cultured in our model. This could be of use in culturing hepatitis B virus, which requires liver specific factors for replication such as sodium taurocholate transporting peptide (NTCP)

receptors [63]. The ability to improve cell differentiation when compared to monolayer cell cultures could prove to be useful, as differentiation of cells in culture systems has been shown to be important with viruses such as human papillomavirus. [64, 65]

6 Conclusion

The fabrication of physiologically relevant organ-on-a-chip models is an apparent, essential next step towards improving drug research and disease modeling in a sustainable manner. Increasing the drug research success rate through more accurate modeling of the internal functions of the body in the pharmaceutical industry will lead to a faster, cheaper, and more effective drug development process. This microfluidic model provides physiological resemblance to the human liver in comparison to traditional cell culture devices, adding to the knowledge of currently existing organ-on-a-chip technology. With optimized tubules that are able to allow for even distribution of media to the cells, this model better resemble the liver sinusoids that allow the nutrients from the blood to evenly reach the surrounding cells. This device therefore leads researchers one step closer to being able to conduct drug testing using an organ-on-a-chip model of the liver that will replicate *in-vivo* cell functions.

This liver model, once successfully tested for cell viability and metabolic activity, could be used in conjunction with other organ-on-a-chip models to test the overall effects of drugs within a system in the body. For example, our proposed liver on a chip model could be combined with existing microfluidic modeling systems, such as the kidney on a chip model, in order to study the effect of a drug on the entire excretory system. It could furthermore be integrated to create body on a chip devices [66, 67, 68, 69]. Additionally, this research model could help eliminate the need for animal

testing by providing a more accurate alternative for human systems. The advancement of therapeutics is impeded by rudimentary drug testing models, and research in this area is the key to accessing the full potential of modern medicinal technology.

7 Appendices

A MATLAB Code

```
clc, clear

format long

Qp = 7.7798*10^-16; %Set the flow rate through the pores ...
    (m^3/s)

%--Define Tube Dimensions Here to Quantify Rt----

L = 10; %Length between pores (um)

Rtube = 17.5; %Inner Radius of the tube (um)

viscosity = 0.6922*10^-3; %Viscosity of water at 37 deg C ...
    (Pa*s)

Rt = (8*viscosity*(L*10^-6))/(pi*((Rtube*10^-6)^4)); ...
    %(N/m^2)/(m^3/s)

%--Define Tube Dimensions Here to Quantify Rl----

Lp = 5; %Thickness of tube wall (um)

Rpore = 0.75; %Radius of the first pore (um)

viscosity = 0.6922*10^-3; %Viscosity of water at 37 deg C ...
    (Pa*s)

Npore_Parallel = 5; %Number of pores at each pore row
```

```

Rpore1 = (8*viscosity*(Lp*10^-6))/(pi*((Rpore*10^-6)^4)); ...
    % (N/m^2) / (m^3/s)

R1 = Rpore1/Npore_Parallel; % (N/m^2) / (m^3/s)

Nmax = 50; %Set Total Number of Pore Rows (Sets of resistors)

R = zeros(1,Nmax);

R(1) = R1; %Set R1

for n = 2:Nmax
    x = ...
        ((Nmax+1-n)*R(n-1) - ((Nmax+2-n)*(Nmax+1-n))/2)*Rt)/(Nmax+2-n); ...
        %Resistance of pore set
    R(n) = x;
end

Rind = R*Npore_Parallel; %Equation for resistance of each ...
    individual pore
indradius = ((8*viscosity*(Lp*10^-6))./(Rind*pi)).^(1/4); ...
    %Equation for radius of each individual pore

Qref = Nmax+1;

Q(Qref) = (R(Nmax)/Rt)*Qp; %Flow rate out of central tubule

for i = 1:Nmax

```

```

q = Qref-i;
qref = q+1;
y = Q(qref)+Qp;
%Q(q) = simplify(y);
Q(q) = y; %Flow rate through central tubule at each ...
    pore row
end

RTot (Nmax) = Rt+(Rt*R(Nmax))/(Rt+R(Nmax)); %Total ...
    equivalent resistance of tubule

RTot_Ref = Nmax-1;

for j = 1:RTot_Ref
    Tot = Nmax-j;
    Totref = Tot+1;
    z = Rt+(RTot (Totref)*R(Tot))/(RTot (Totref)+R(Tot));
    RTot (Tot) = z; %Total equivalent resistance at each ...
        pore row
end

rowresistance = R %Outputs the total resistance at each ...
    pore row (N/m^2)/(m^3/s)

poreresistance = Rind %Outputs the resistance of the ...
    individual pores at each pore row (N/m^2)/(m^3/s)

flowrate = Q %Outputs the flow rate in the intermediate ...
    tube section at each pore row (m^3/s)

```

```

totalresistance = RTot %Outputs the total equivalent ...
    resistance at each pore row (N/m^2)/(m^3/s)

dp = Q(1)*RTot(1) %Pressure differential (inlet-outlet) of ...
    central tube (N/m^2)

radii = indradius %Radius of the individual pores at each ...
    pore row (m)

Q1 = Q(1) %Input flow rate into central tubule (m^3/s)

```

8 Glossary

Albumin - A globular protein that is produced by the liver that is integral to maintaining oncotic pressure and the transportation of drugs and hormones.

Black Box Warning - Warning placed by the FDA indicating that there are serious risks associated with the drug.

Central vein - Receives blood that has been filtered through the lobule and returns it to the heart for recirculation.

Computer-Aided Design - The use of computer software to virtually design and create object models.

Cyclic olefin copolymer - A clear amorphous polymer with a low moisture absorption rate and is very resistance to acids and bases.

Enzyme-Linked Immunosorbent Assay (ELISA) - A biochemical assay which can detect an antigen in a sample.

Extrusion Based Printing - Depositing of material point by point through a nozzle.

Fenestrated endothelium - A layer of endothelial cells containing small pores that allow for the exchange of molecules between blood in the sinusoids and the hepatic cords.

High Throughput Screening - An assay method to test many reactions systematically and efficiently.

Hepatocytes - Cells of the main parenchymal tissue of the liver that are involved in the liver's most important functions. Make up 70-85% of

the liver's mass.

Hepatic cord - A mass of hepatocytes arranged in a radiating fashion outward from the central vein of the liver lobule.

Hypoxic - A condition in which the tissues are deprived of adequate oxygen supply.

In vitro - Performing a test using living cells outside of the organism.

In vivo - A test performed inside of a living organism.

Laser Lithography - A type of stereolithography that uses short laser pulses to polymerize photosensitive material, revealing only the desired 3D structure.

Live Dead Assay - A chemical test used to quantify cell life through staining living cells one color and dead cells another.

Lobule - A small, repeating subunit of the liver composed of hepatocytes that filters incoming blood.

Microfluidic Device - A cell culture device with a set of microchannels etched in that allows for control of the fluid flowing through the channels.

Nanoscribe - A 3D printer that uses laser lithography techniques to print in dimensions as small as nanoscale.

Organ-on-a-Chip - A 3D microfluidic cell culture chip that can represent the functions and physiological responses of an organ.

OrmoComp - A biocompatible gel with high chemical and thermal stability.

Paracrine Signaling - A form of cell communication where one cell produces a signal to alter the behavior or differentiation of nearby cells.

Photocurable resin - A substance that is hardened when exposed to ultraviolet light.

Photolithography - Microfabrication process to transfer intricate geometries on a mask to a silicon wafer.

Photopolymer - A polymer that changes properties when exposed to light.

Photoresist - Substrate that is chemically cured through contact with UV light.

Photomask - An opaque substrate with patterned transparencies, designed to allow UV light shine through in a defined way.

Piezo-actuators - Converts electrical energy into mechanical energy to allow for precise movement, with submicron scale accuracy, in positional based systems.

Polycarbonate - Plastic used to create strong tough materials that are often clear.

Polydimethylsiloxane - Biocompatible silicon substrate.

Polyjet Printing - Dispenses microdroplets of photopolymers to create a 3D object.

Portal vein - Blood vessel that carries nutrient-rich blood from the gastrointestinal tract and spleen to the liver.

Sinusoids - Small blood vessels that permeate the liver lobule to allow blood flow throughout the liver.

Stereolithography - 3D printing technique that uses focused light to cure liquid polymers and create 3D structures.

References

- [1] Mohs, R. C. & Greig, N. H. Drug discovery and development: Role of basic biological research. *Alzheimer's & Dementia : Translational Research & Clinical Interventions* **3**, 651–657 (2017).
- [2] Cook, D. *et al.* Lessons learned from the fate of AstraZeneca's drug pipeline: a five-dimensional framework. *Nature Reviews Drug Discovery* **13**, 419 (2014).
- [3] Saxena, R., Theise, N. D. & Crawford, J. M. Microanatomy of the human liver-exploring the hidden interfaces. *Hepatology (Baltimore, Md.)* **30**, 1339–1346 (1999).
- [4] Wambaugh, J. & Shah, I. Simulating microdosimetry in a virtual hepatic lobule. *PLoS computational biology* **6**, e1000756 (2010).
- [5] Braet, F. & Wisse, E. Structural and functional aspects of liver sinusoidal endothelial cell fenestrae: a review. *Comparative Hepatology* **1**, 1 (2002).
- [6] Bhatia, S. N. & Ingber, D. E. Microfluidic organs-on-chips. *Nature Biotechnology* **32**, 760–772 (2014).
- [7] Lamont, A. C., Alsharhan, A. T. & Sochol, R. D. Geometric Determinants of In-Situ Direct Laser Writing. *Scientific Reports* **9**, 394 (2019).

- [8] Hartung, T. & Daston, G. Are In Vitro Tests Suitable for Regulatory Use? *Toxicological Sciences* **2**, 233–237 (2009).
- [9] Astashkina, A., Mann, B. & Grainger, D. W. A critical evaluation of in vitro cell culture models for high-throughput drug screening and toxicity. *Pharmacology & Therapeutics* **134**, 82–106 (2012).
- [10] Ghabril, M., Chalasani, N. & Bjornsson, E. Drug-induced liver injury: a clinical update. *Current Opinion in Gastroenterology* **26**, 222–226 (2010).
- [11] Borlak, J., Chougule, A. & Singh, P. K. How useful are clinical liver function tests in in vitro human hepatotoxicity assays? *Toxicology in Vitro* **28**, 784–795 (2014).
- [12] Roskams, T. A. *et al.* Nomenclature of the finer branches of the biliary tree: canals, ductules, and ductular reactions in human livers. *Hepatology (Baltimore, Md.)* **39**, 1739–1745 (2004).
- [13] Marieb, E. N. & Hoehn, K. *Anatomy & physiology* (Pearson/Benjamin Cummings, Upper Saddle River, NJ, 2011), 4th ed edn.
- [14] Chambard, M., Verrier, B., Gabrion, J. & Mauchamp, J. Polarity reversal of inside-out thyroid follicles cultured within collagen gel: re-expression of specific functions. *Biology of the Cell* **51**, 315–325 (1984).
- [15] Huh, D. *et al.* Reconstituting organ-level lung functions on a chip. *Science (New York, N.Y.)* **328**, 1662–1668 (2010).

- [16] Agarwal, A., Goss, J. A., Cho, A., McCain, M. L. & Parker, K. K. Microfluidic heart on a chip for higher throughput pharmacological studies. *Lab on a Chip* **13**, 3599 (2013).
- [17] Marx, V. Tissue engineering: Organs from the lab. *Nature* **522**, 373–377 (2015).
- [18] Cirit, M. *et al.* Human physiome on a chip: A platform for drug discovery and development. *Toxicology Letters* **258**, **Supplement**, S191–S192 (2016).
- [19] Huh, D. *et al.* A Human Disease Model of Drug Toxicity-Induced Pulmonary Edema in a Lung-on-a-Chip Microdevice. *Science Translational Medicine* **4**, 159ra147–159ra147 (2012).
- [20] Lee, J. M., Zhang, M. & Yeong, W. Y. Characterization and evaluation of 3d printed microfluidic chip for cell processing. *Microfluidics and Nanofluidics* **20**, 5 (2016).
- [21] Mammoto, T., Mammoto, A. & Ingber, D. E. Mechanobiology and developmental control. *Annu Rev Cell Dev Biol* **29**, 27–61 (2013).
- [22] Ma, C. *et al.* On-Chip Construction of Liver Lobule-like Microtissue and Its Application for Adverse Drug Reaction Assay. *Analytical Chemistry* **88**, 1719–1727 (2016).
- [23] Duffy, D. C., McDonald, J. C., Schueller, O. J. & Whitesides, G. M. Rapid Prototyping of Microfluidic Systems in Poly(dimethylsiloxane). *Anal Chem* **70**, 4974–84 (1998).

- [24] Mersch-Sundermann, V., Knasmüller, S., Wu, X.-j., Darroudi, F. & Kassie, F. Use of a human-derived liver cell line for the detection of cytoprotective, antigenotoxic and cogenotoxic agents. *Toxicology* **198**, 329–340 (2004).
- [25] Marion, M.-J., Hantz, O. & Durantel, D. The HepaRG Cell Line: Biological Properties and Relevance as a Tool for Cell Biology, Drug Metabolism, and Virology Studies. In Maurel, P. (ed.) *Hepatocytes*, no. 640 in *Methods in Molecular Biology*, 261–272 (Humana Press, 2010).
- [26] Lee, S.-A. *et al.* Spheroid-based three-dimensional liver-on-a-chip to investigate hepatocyte-hepatic stellate cell interactions and flow effects. *Lab on a Chip* **13**, 3529–3537 (2013).
- [27] Lee, J. *et al.* A 3d alcoholic liver disease model on a chip. *Integrative Biology* **8**, 302–308 (2016).
- [28] Mao, S., Gao, D., Liu, W., Wei, H. & Lin, J. M. Imitation of drug metabolism in human liver and cytotoxicity assay using a microfluidic device coupled to mass spectrometric detection. *Lab Chip* **12**, 219–26 (2012).
- [29] Choucha-Snouber, L. *et al.* Investigation of ifosfamide nephrotoxicity induced in a liver–kidney co-culture biochip. *Biotechnology and Bioengineering* **110**, 597–608 (2013).
- [30] Wagner, I. *et al.* A dynamic multi-organ-chip for long-term cultivation

- and substance testing proven by 3d human liver and skin tissue co-culture. *Lab on a Chip* **13**, 3538 (2013).
- [31] Maschmeyer, I. *et al.* A four-organ-chip for interconnected long-term co-culture of human intestine, liver, skin and kidney equivalents. *Lab Chip* **15**, 2688–2699 (2015).
- [32] Zhang, C., Zhao, Z., Abdul Rahim, N. A., van Noort, D. & Yu, H. Towards a human-on-chip: Culturing multiple cell types on a chip with compartmentalized microenvironments. *Lab on a Chip* **9**, 3185 (2009).
- [33] Murphy, S. V. & Atala, A. 3d bioprinting of tissues and organs. *Nature Biotechnology* **32**, 773–785 (2014).
- [34] Gao, Q., He, Y., Fu, J.-z., Liu, A. & Ma, L. Coaxial nozzle-assisted 3d bioprinting with built-in microchannels for nutrients delivery. *Bio-materials* **61**, 203–215 (2015).
- [35] Sochol, R. D., Gupta, N. R. & Bonventre, J. V. A Role for 3d Printing in Kidney-on-a-Chip Platforms. *Current Transplantation Reports* **3**, 82–92 (2016).
- [36] Therriault, D., White, S. R. & Lewis, J. A. Chaotic mixing in three-dimensional microvascular networks fabricated by direct-write assembly. *Nature Materials* **2**, 265–271 (2003).
- [37] Biglino, G., Verschueren, P., Zegels, R., Taylor, A. M. & Schievano, S. Rapid prototyping compliant arterial phantoms for in-vitro studies

- and device testing. *Journal of Cardiovascular Magnetic Resonance* **15**, 2 (2013).
- [38] Au, A. K., Bhattacharjee, N., Horowitz, L. F., Chang, T. C. & Folch, A. 3d-printed microfluidic automation. *Lab Chip* **15**, 1934–1941 (2015).
- [39] Soman, P. *et al.* Cancer cell migration within 3d layer-by-layer microfabricated photocrosslinked PEG scaffolds with tunable stiffness. *Biomaterials* **33**, 7064–7070 (2012).
- [40] Klein, F. *et al.* Elastic Fully Three-dimensional Microstructure Scaffolds for Cell Force Measurements. *Advanced Materials* **22**, 868–871 (2010).
- [41] Nanoscribe. 3d printing on the micrometer scale - Nanoscribe GmbH.
- [42] Ruszaj, A. Some Aspects of Bioinspirations in Energy Production and Consumptions. *Procedia Engineering* **157**, 465–471 (2016).
- [43] Silva, J. V. L. & Rezende, R. A. Additive Manufacturing and its future impact in logistics. *IFAC Proceedings Volumes* **46**, 277–282 (2013).
- [44] Ostendorf, A., Chichkov, B. & Hannover, L. Two-Photon Polymerization: A New Approach to Micromachining.
- [45] Schizas, C. & Karalekas, D. Mechanical characteristics of an Ormocomp® biocompatible hybrid photopolymer. *Journal of the Mechanical Behavior of Biomedical Materials* **4**, 99–106 (2011).

- [46] Mukhopadhyay, R. When PDMS isn't the best. *Analytical Chemistry* **79**, 3248–3253 (2007).
- [47] Nakamura, M., Iwanaga, S., Henmi, C., Arai, K. & Nishiyama, Y. Biomatrices and biomaterials for future developments of bioprinting and biofabrication. *Biofabrication* **2** (2010).
- [48] Klapperich, C. M. Microfluidic diagnostics: time for industry standards. *Expert Review of Medical Devices* **6**, 211–213 (2009).
- [49] Fluigent applications of organ-on-a-chip platform.
- [50] MFCS™-EZ Microfluidic Flow Control System.
- [51] Frp flow sensor (2018).
- [52] DeLeve, L. D. Liver sinusoidal endothelial cells and liver regeneration. *The Journal of Clinical Investigation* **123**, 1861–1866 (2013).
- [53] Alastair D Burt, Portmann, B., Ferrell, L. & MacSween, R. M. N. *MacSween's Pathology of the Liver* (Churchill Livingstone/Elsevier, Philadelphia, PA, 2007), 5 edn.
- [54] Nanoscribe IP-resist.
- [55] Käpylä, E. *et al.* Ormocomp-modified glass increases collagen binding and promotes the adherence and maturation of human embryonic stem cell-derived retinal pigment epithelial cells. *Langmuir: the ACS journal of surfaces and colloids* **30**, 14555–14565 (2014).
- [56] Ormocomp. OrmoComp® | micro resist technology GmbH.

- [57] Choi, S., Sainz, B., Corcoran, P., Uprichard, S. & Jeong, H. Characterization of increased drug metabolism activity in dimethyl sulfoxide (DMSO)-treated Huh7 hepatoma cells. *Xenobiotica* **39**, 205–217 (2009). URL <http://www.tandfonline.com/doi/full/10.1080/00498250802613620>.
- [58] Zhou, Q. *et al.* Liver injury-on-a-chip: microfluidic co-cultures with integrated biosensors for monitoring liver cell signaling during injury. *Lab on a Chip* **15**, 4467–4478 (2015).
- [59] Esch, M. B., Ueno, H., Applegate, D. R. & Shuler, M. L. Modular, pumpless body-on-a-chip platform for the co-culture of GI tract epithelium and 3d primary liver tissue. *Lab on a Chip* **16**, 2719–2729 (2016).
- [60] Kuhns, D. B., Nelson, E. L., Alvord, W. G. & Gallin, J. I. Fibrinogen induces IL-8 synthesis in human neutrophils stimulated with formyl-methionyl-leucyl-phenylalanine or leukotriene B(4). *Journal of Immunology (Baltimore, Md.: 1950)* **167**, 2869–2878 (2001).
- [61] Brockmöller, J. & Roots, I. Assessment of liver metabolic function. Clinical implications. *Clinical Pharmacokinetics* **27**, 216–248 (1994).
- [62] Maher, J. J. Exploring alcohol’s effects on liver function. *Alcohol Health and Research World* **21**, 5–12 (1997).
- [63] Hayes, C. N. & Chayama, K. HBV culture and infectious systems. *Hepatology International* **10**, 559–566 (2016).

- [64] Steinbach, A. & Riemer, A. B. Immune evasion mechanisms of human papillomavirus: An update. *International Journal of Cancer* **142**, 224–229 (2018).
- [65] Ryndock, E. J., Biryukov, J. & Meyers, C. Replication of Human Papillomavirus in Culture. In Keppler, D. & Lin, A. W. (eds.) *Cervical Cancer: Methods and Protocols*, Methods in Molecular Biology, 39–52 (Springer New York, New York, NY, 2015).
- [66] Esch, M. B., King, T. L. & Shuler, M. L. The role of body-on-a-chip devices in drug and toxicity studies. *Annual Review of Biomedical Engineering* **13**, 55–72 (2011).
- [67] Esch, M. B. *et al.* On chip porous polymer membranes for integration of gastrointestinal tract epithelium with microfluidic 'body-on-a-chip' devices. *Biomedical Microdevices* **14**, 895–906 (2012).
- [68] Williamson, A., Singh, S., Fernekorn, U. & Schober, A. The future of the patient-specific Body-on-a-chip. *Lab on a Chip* **13**, 3471–3480 (2013).
- [69] Skardal, A., Shupe, T. & Atala, A. Organoid-on-a-chip and body-on-a-chip systems for drug screening and disease modeling. *Drug Discovery Today* **21**, 1399–1411 (2016).